1972

A study of the effect of drilled holes on the concentration of elastic stresses around a notch

Glenn Michael Kmecz

Department:

A STUDY OF THE EFFECT OF DRILLED HOLES ON THE CONCENTRATION OF ELASTIC STRESSES AROUND A NOTCH

BY

GLENN MICHAEL KMECZ, 1947-

A THESIS

Presented to the Faculty of the Graduate School of the

UNIVERSITY OF MISSOURI-ROLLA

In Partial Fulfillment of the Requirements for the Degree

MASTER OF SCIENCE IN ENGINEERING MECHANICS

1972

Approved by

Peter G. Hansen (Advisor) Edward E. Harmsey

Jerry F. Lehnhoff

ABSTRACT

Hole drilling as a method for improving the toughness of notch weakened tensile specimens is investigated by means of a photoelastic technique. Tests were performed on 20%, 40%, 60%, and 80% notch depth specimens machined from PSM-1 photoelastic material. The basic criteria for success was no increase in the elastic stress concentration factor. The photoelastic results were verified by a finite element stress analysis of the 60% notch depth specimens. Comparison of the experimental and numerical results provide conclusive proof that no increase in the elastic stress concentration factor occurs when proper positioning of the drilled holes is accomplished.

ACKNOWLEDGEMENT

The author wishes to express his appreciation to his advisor, Professor Peter G. Hansen, for his guidance and motivation during the preparation of this manuscript and his entire graduate program.

The writer wishes to thank Assistant Professor Edward E. Hornsey and Associate Professor Terry F. Lehnhoff for their participation on the examining committee and also Assistant Professor Edward J. Beckemeyer for his comments and suggestions.

Special thanks are in order for Mr. Wilson Sherrill, who machined and helped redesign many parts for the experiment and also for his encouragement and persistant help during the testing. Gratitude is also extended to Mr. Marvin Vogeler for an excellent job of machining the photoelastic templates.

The typing of the manuscript was done by Mrs. Alice Crangle to whom I am deeply indebted for a job well done.

Finally, I wish to express deepest thanks to my parents Andrew and Dolores Kmecz, for their understanding and financial assistance, without which this thesis would not have been possible.

TABLE OF CONTENTS

Page

LIST OF ILLUSTRATIONS

Figure Page

LIST OF TABLES

NOMENCLATURE

A	notch depth in single-edge-notch specimen
A°	angstrom, one hundred-millionth (10^{-8}) of a centimeter
A_{nom}	gross cross sectional area of SEN specimen
ASA	photographic term used in conjunction with film speed
A/W	ratio of notch depth, A, to specimen width, W, in percent
b	Burgers vector of a dislocation
c	one-half the length of an internal crack or the length of crack exposed to the surface
d_a	actual distance for close-up photographs
d_p	photographic distance for close-up photographs
D	one-half the crystallographic grain size
D_a	actual distance for full-view photographs
D_p	photographic distance for full-view photographs
E	modulus of elasticity
F	photoelastic material fringe constant
h	thickness of photoelastic specimen
I	moment of inertia
K	parameter that determines grain-size dependence of fracture strength
K_σ	elastic stress concentration factor
L	single-edge-notch specimen length
M	bending moment
n	isochromatic fringe order
P	specimen load
R	computer program notation for X-direction

SEN	single-edge-notch
$S.F._{cu}$	scale factor for close-up photographs
$S.F._{fv}$	scale factor for full-view photographs
W	single-edge-notch specimen width
X	distance across plane of notch symmetry from specimen edge
y	distance from neutral axis for bending stress calculations
Y	distance from plane of notch symmetry
Z	computer program notation for Y-direction
α	coefficient of thermal expansion
γ_s	true surface energy or elastic work
γ_p	plastic work done near the tip of a moving micro or macro crack
ε	strain
$\lambda/4$	one-quarter wave (i.e. $\lambda/4$-plate)
μ	one-millionth (10^{-6})
υ	Poisson's ratio
ρ	notch root radius
σ	applied tensile or compressive stress
σ_f	fracture stress of initially flaw free specimen
σ_F	fracture stress of large structure containing a flaw
σ_i	frictional stress resisting motion of an unlocked dislocation
σ_m	stress required to keep moving crack in motion
σ_{max}	maximum stress at the tip of a notch or crack
σ_{nom}	nominal stress applied over the gross cross sectional area
σ_N	bending stress
σ_y	yield stress

$\sigma_1-\sigma_2$	principal stress difference
τ_s	critical resolved shear stress at which yielding occurs near piled-up group of dislocations
ω	notch flank angle

I. INTRODUCTION

The increasing emphasis on fracture mechanics technology has produced a significant impact in the field of materials science. New principles and methods are frequently being introduced, which aid the engineer in coping with problems involved in fracture and fatigue.

Many structural failures have resulted from the presence of a notch or crack introduced either by design or error. Previous work by Tetelman and Rau (1) has indicated that two small holes drilled near the root of a Charpy type V-notch, have successfully produced a significant increase in the notch toughness of such specimens. A brief review of the mechanics involved is necessary at this point to clarify this phenomena.

According to Tetelman and Rau (2) a material free from flaws exhibits plastic deformation when the applied stress equals the yield strength of the material. Exclusive of low temperature failure, this applied stress is less than that of the cleavage fracture stress. Strain hardening, as a result of plastic deformation leads to cleavage fractures. While temperature has very little effect on a material's cleavage fracture strength, the yield strength decreases with increasing temperature. At higher temperatures then, the amount of strain hardening and also the cleavage fracture strain are increased to a point where the material fails by ductile tearing instead of brittle cleavage. Only materials of the face centered cubic crystal structure, such as aluminum and copper, do not exhibit this brittle to ductile transition at higher temperature.

Dieter (3) suggests that a notch in a material produces a significant increase in the brittle to ductile transition temperature. The presence of the notch produces a stress concentration. As the loading is increased beyond the yield point, plastic deformation produces plastic constraint at the root of the notch. The presence of the notch causes cleavage of the material at a temperature which an unnotched material would be ductile. Tetelman and Rau (2) give two reasons for this behavior. First, the triaxial state of stress at the root of the notch causes an increase in the tensile yield strength, which consequently reduces the amount of strain hardening required to produce cleavage fracture. Secondly, the strain is concentrated at the notch root, therefore, the net strain needed to produce the required strain hardening is less. As the root radius of the notch is decreased, these effects change drastically.

To improve the toughness of notch weakened members, Tetelman and Rau (2) suggest that two small holes drilled above and below the notch root, sufficiently reduce the plastic constraint. Using impact, slow bend, and tension tests over a wide temperature range, Rau (4) was able to improve the strength of notch weakened members. The strain concentration produced between the holes and the edge of the notch, causes ductile tearing there before brittle cleavage can occur. This effect is more pronounced than that produced by drilling a single hole at the notch root, since the two hole method causes a larger degree of plastic blunting. The two hole method has another distinct advantage in that it does not change the elastic stress concentration factor as the single hole method does.

Testing (1) was primarily directed at iron base alloys, such as 3% silicon iron and mild steel. The position and size of the holes were varied until the optimum results were obtained for most variations in notch geometry. Dislocation etch pitting provided a convenient technique by which to study the effects of the holes on the plastic strain distribution. Using this technique the optimum hole location was found to be inside the yield zones which emanate from the notch root at the onset of plastic deformation.

Another paper written by Tetelman and Rau (5) discusses the results of a photoelastic study to observe the effects of the hole drilling on the elastic stress concentration factor. A bending test was used to demonstrate this effect. Results concluded no significant change in the elastic stress concentration factor between the drilled and undrilled specimens.

Tetelman and Rau (2) conclude their results by indicating that "...designs for improving notch toughness should be based on a maximum redistribution of plastic strain around the notch tip rather than solely on a reduction of the elastic stress concentration."

The purpose of this investigation is to further provide conclusive proof that no significant increase in the elastic stress concentration factor results when proper positioning of the holes is employed. The present study was performed on a single-edge-notched specimen subjected to an axial tensile load. The optimum hole size established by Rau (2) for the standard Charpy V-notch was used for all specimens containing the holes. The depth of the notch was varied from 20% to 80% of the plate width, while the root radius and flank angle

were kept the same as those of the Charpy V-notch. Photoelasticity was used as an experimental technique, while finite element stress analysis provided an analytical comparison.

II. REVIEW OF LITERATURE

The study of fracture mechanics is a relatively new field, originating with Griffith (6,7) around 1920, with the publication of the theory of elastic crack propagation. In this presentation, Griffith hypothesized that unstable elastic crack propagation results from a decrease in the free energy of a system. For a completely brittle solid, elastic crack propagation initiates when

$$\sigma = \sigma_F = \sqrt{\frac{2E\gamma_s}{\pi c}}$$

Later work by Orowan (8,9,10) and Irwin (11) demonstrated that localized plastic deformation accompanies crack propagation. Some plastic work, γ_p, is then required to move the crack in conjunction with the elastic work, γ_s, needed to create the two new fracture surfaces. The Griffith equation was modified to read (in plane stress)

$$\sigma_m = \sqrt{\frac{2E(\gamma_s+\gamma_p)}{\pi c}}$$

Further investigation by Zener (12) around 1948 brought out the fact that high stresses at the head of a dislocation pile-up could cause fracture.

Stroh (13) in 1954 established, using the Griffith equation and the dislocation pile-up theory, that a resolved shear stress, τ_s, was responsible for cleavage when acting upon n dislocations to satisfy the equation

$$nb\tau_s = 12\gamma$$

where b is the Burgers vector and γ is the surface energy. However, Petch (14) found that for iron and steel the equation

$$\sigma_f = \sigma_i + KD^{-1/2}$$

agrees well with experimental data.

Cottrell (15) in 1958 discussed another mechanism by which cleavage fracture could occur by the glide of dislocations on intersecting slip planes. This mechanism is favorable from an energy standpoint for body centered cubic and hexagonal close packed crystal structures. Experimental work verifies that face centered cubic materials, such as aluminum and copper, do not exhibit brittle cleavage fractures.

Many significant contributions concerning the mechanics of fracture have since been published. However, few noteworthy advances were made in the formulation of an exact method for calculating the stresses around a notch or crack until 1958, when Neuber (16) published his work in this area. Previous formulation was based on two assumptions. First, that the structure or part to be analyzed was usually represented by a simple bar, the stress distribution for which was found from elementary formulas. Secondly, that the elastic behavior of the structure could be compared to the behavior of an ideal Hookian material. These assumptions led to many discrepancies. Neuber developed new methods for analyzing the effects of surface contours, nonlinear elasticity, and many other factors, which were previously oversimplified.

Metallurgical variables (17), such as heat treatment, alloying, and forming, along with mechanical methods of crack abatement (18) and detection (19,20) have provided the engineer with a vast amount of information with which to design so that fracture will not occur. One such technique as developed by Tetelman and Rau (1) is the subject of this discussion.

Until recently, the design engineer and the materials scientist possessed different viewpoints as to the concepts of fracture. The engineer often lacked the knowledge of the microscopic aspects of fracture, while the materials scientist very seldom appreciated the macroscopic viewpoint. A realization of this knowledge void led Tetelman and McEvily (18) to publish their work in 1967 correlating the two areas of study.

III. TEST EQUIPMENT

A standard circular polariscope (Figure 1) was used for the calibration and photoelastic study. The light originates from the source at the rear of the lenses and passes through a sodium yellow filter to produce monochromatic light with a wavelength of approximately 5460 A°. After passing through the filter, the light enters a collimating lens, which produces a parallel stream of light. The light then passes through the polarizer, first quarter-wave plate, model, second quarter-wave plate, and analyzer. After leaving the analyzer it is focused, by means of a field lens, on an opaque glass plate, upon which is inscribed a grid network of 1/4" squares.

The circular polariscope differs from the plane polariscope by the addition of the quarter-wave plates, which are incorporated to remove the isoclinics (principal stress directions) from the image.

The standard 5x7 camera mounted on the polariscope was not capable of providing sufficient detail of the fringe order at the notch root. For this reason, a Nikon F 35mm camera was adapted for use with the polariscope. A 43mm to 86mm zoom lens used in conjunction with a bellows provided accurate detail at the notch root of the specimen. For the full view pictures, a 135mm lens was used with the bellows and a tripod. All photographs used in the analysis were taken with Kodak Plus-X Pan film which has a speed of 125 ASA.

The test specimen was loaded by means of a Dillon universal testing machine. A Dillon 500 pound capacity strain gage dynamometer mounted on top of the testing machine was used to indicate the load. The dynamometer consists of a carefully machined cantilevered beam,

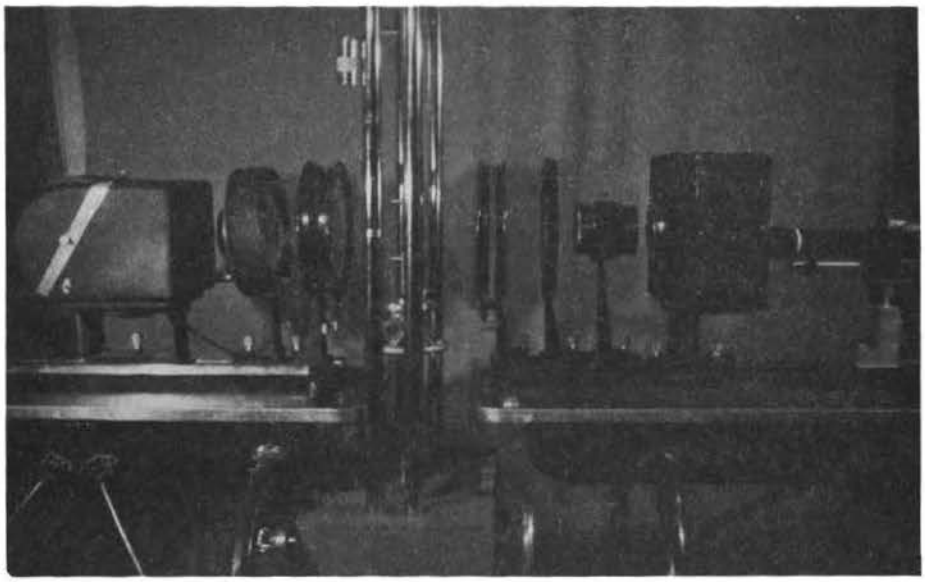

Figure 1. Standard Circular Polariscope

to which are fastened two etched foil strain gages on each of the upper and lower surfaces. This comprises a four active-arm temperature-compensated strain gage bridge. The unconstrained end of the beam rests on a pivot. As load is applied to the center of the beam the upper set of gages is placed in compression and the lower set in tension. This produces an unbalance in the strain gage bridge, the electrical output of which is proportional to the applied load. This output is sent through a shielded cable to the Dillon strain gage meter readout where the applied load may be read directly from the dial.

The testing machine was placed in its proper position in relation to the polariscope (Figure 1).

Machining of all specimens was accomplished using two Chapman photoelastic model-making routers of 45,000 and 22,000 rpm.

A Tinius Olsen universal testing machine was used for the strength testing, along with a Budd portable strain indicator for measuring the strain gage output.

IV. TEST SPECIMENS

The discussion of the specimens used in this analysis is divided into three parts. Principal considerations are the material properties, specimen design, and machining.

A. Material

1. Strength Tests

The material used for the test specimens was chosen on the basis of the strength tests and fracture mode. Twelve specimens were made and tested before suitable results were obtained. Strength tests 1 through 7 were performed on CR-39 photoelastic material from Photolastic Incorporated. Several specimen designs were tried, but due to the great degree of difficulty encountered in the machining, testing, and evaluation of results of CR-39, it was decided that a new material was needed.

As an alternative, PSM-1 was selected due to its superior machining capabilities and also its ability to deform plastically. The highly brittle fractures exhibited by the CR-39 showed it to be somewhat impractical for the results which were intended. Therefore, the PSM-1 proved to be superior to CR-39 in two areas.

(1) Due to its greater ductility, PSM-1 is easily machined with less possibility of stress concentrations due to chipping.

(2) Also due to the greater ductility of PSM-1 it is better suited for the studies which follow. Plastic deformation, which is an important mechanism in fracture, is very predominant in the PSM-1, whereas it is practically non-existant in the CR-39.

Strength tests 8 through 11 yielded inconclusive results due primarily to strain gage failures. A Micro-Measurements high elongation type strain gage was used for strength test number twelve and provided excellent results (Figure 2).

The test specimen number twelve (Figure A-1) was carefully machined and the strain gage mounted using Eastman 910 cement. The specimen was placed in the Tinius Olsen testing machine and the Budd strain indicator was attached to the strain gage leads. The results from this test (Table A-1) and the stress-strain curve for the PSM-1 (Figure A-2) are shown in Appendix A along with calculations for the modulus of elasticity and yield strength. The properties shown in Figure 2 were found from the strength test calculations.

2. Calibration

The purpose of the calibration test was to determine the photoelastic fringe constant, F, of the material. The test was performed on a 2-3/4" diameter disc (Figure A-3) machined from 1/4" thick PSM-1 sheet obtained from Photolastic Incorporated.

The disc was loaded in diametral compression on the Dillon universal testing machine according to the method outlined by Durelli and Riley (21).

Stress values were calculated at two points along the horizontal diameter of the specimen. Calibration data (Table A-2) and the resulting calibration curves (Figures A-4, A-5) are presented in the appendix. The material fringe constant, F, was calculated (Appendix A) and found to be 37.824 psi-in/fringe, which agrees well with the value of 40 psi-in/fringe as given in the manufacturers literature.

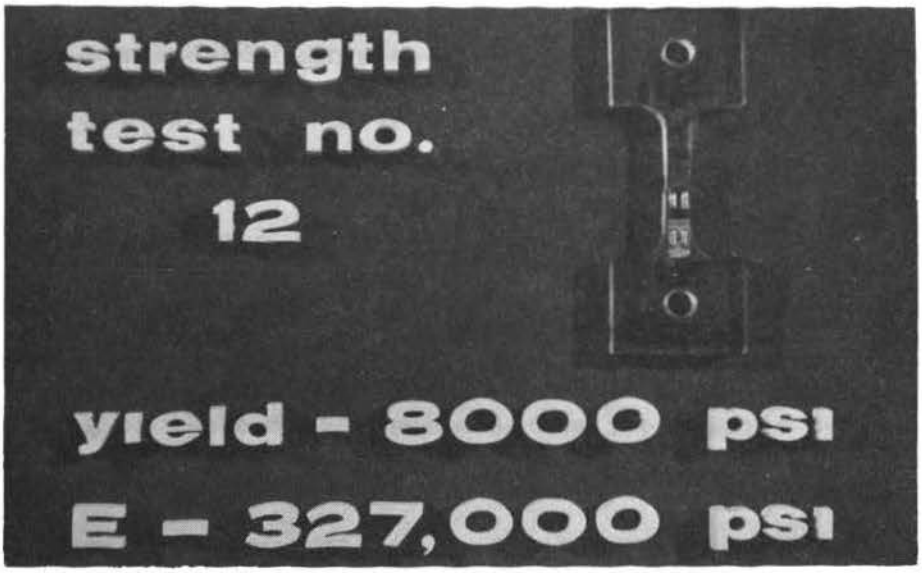

Figure 2. Strength Test Number 12 Material Properties and Specimen

B. Design of Notched Specimens

A single-edge-notch (SEN) tension member (Figure 3) was used for all notched specimens. Pook and Dixon (22) have indicated this type of configuration to be very well suited to fracture toughness studies.

The basic notch geometry (Figure 4), except for the notch depth, A, remained the same as that used in the photoelastic bending study performed by Tetelman and Rau (5). All dimensions were 5 times larger than that of a standard Charpy specimen in order to give good photographic results. The optimum hole size and location as established by Tetelman and Rau (1) was used for all specimens for which holes were intended (Figures 4 and 5). A complete listing of all notched specimens and their respective dimensions is presented in Table 1.

C. Machining of Notched Specimens

Machining of the notched specimens was implemented by the use of templates. Four templates were designed, one to represent each of the four notch depths. Aluminum of 0.100 inch thickness was used for the templates. Machining, including boring and positioning of the holes, was performed using a Bridgeport vertical milling machine.

The templates were fastened to a one-fourth inch thick sheet of PSM-1 by means of Scotch double stick tape and remained attached during the entire machining operation. Each specimen was rough cut from the sheet on a band saw. The specimen was placed on the router table with the aluminum template on the bottom. A steel plug was threaded into the router table directly beneath the cutter, leaving

Material - PSM-1
Thickness - 1/4"
Scale - 1:1

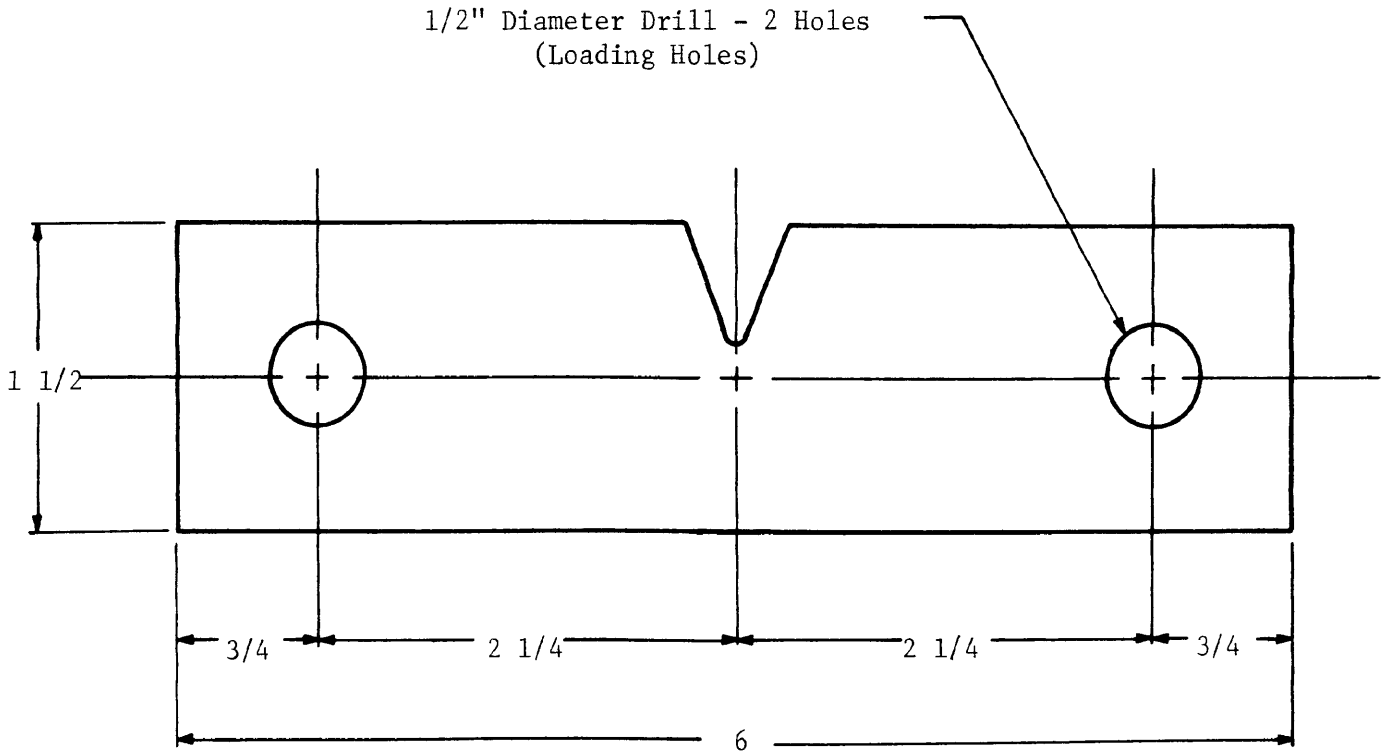

Figure 3. Single-Edge-Notch Tension Specimen

SCALE - 5:1

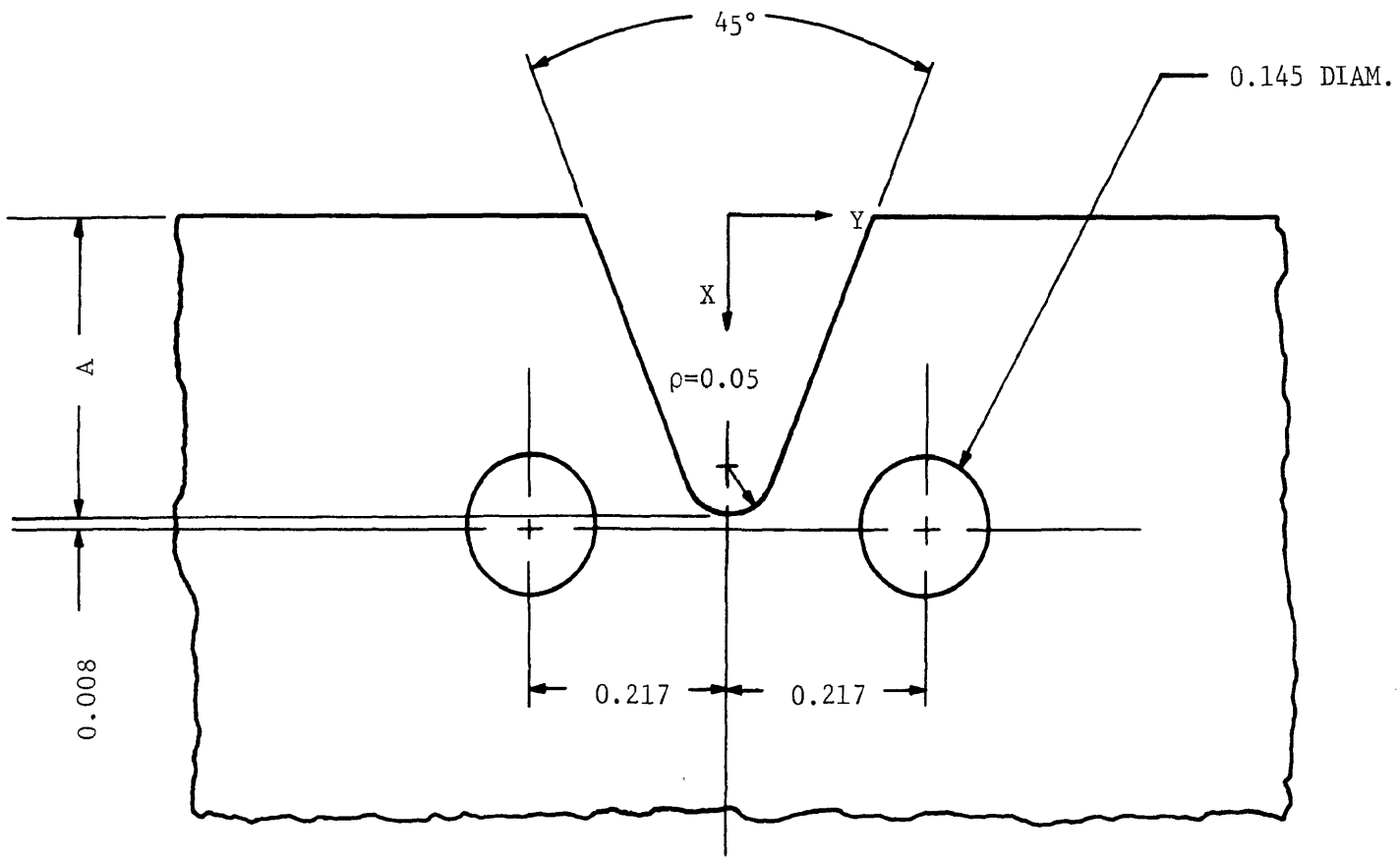

Figure 4. Basic Notch Geometry

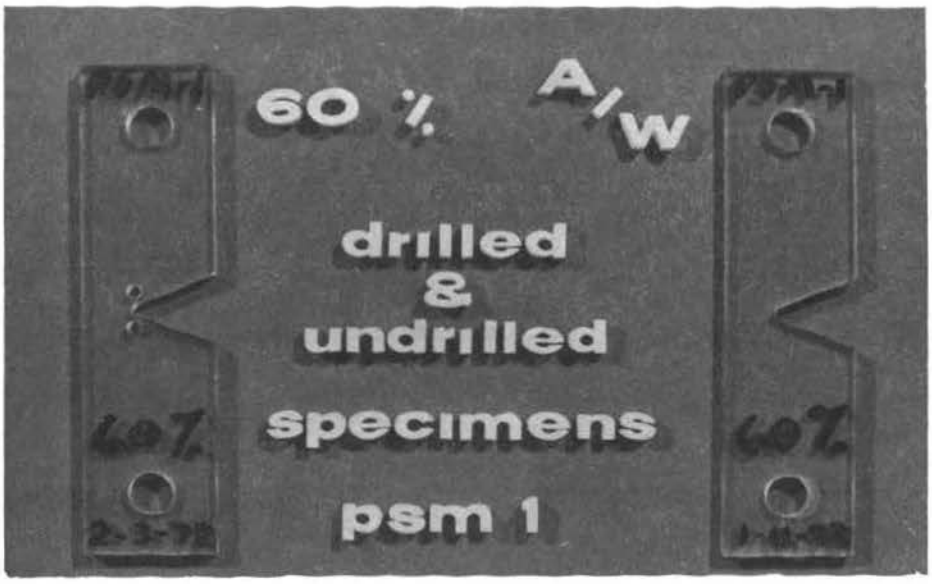

Figure 5. Notched Tensile Specimens

TABLE I

Notched Specimen Dimensions

Specimen % A/W	Length (inches) L	Width (inches) W	Notch Depth (inches) A	Flank Angle (degrees) ω	Root Radius (inches) ρ
20 drilled	6.0	1.5	0.3	45	0.050
20 undrilled	6.0	1.5	0.3	45	0.050
40 drilled	6.0	1.5	0.6	45	0.050
40 undrilled	6.0	1.5	0.6	45	0.050
60 drilled	6.0	1.5	0.9	45	0.050
60 undrilled	6.0	1.5	0.9	45	0.050
80 drilled	6.0	1.5	1.2	45	0.050
80 undrilled	6.0	1.5	1.2	45	0.050

a few thousandths of an inch clearance between their ends. The plug protruded above the router table to a height equal to the thickness of the aluminum template. The template was guided along the plug by hand allowing the cutter to shave off the excess material to give the PSM-1 the same shape as the template (Figure 6). A plug slightly larger than the cutter was used to make the first cut on the 22,000 rpm router. The 45,000 rpm router was fitted with a plug of the same size as the cutter, which enabled the specimen to be cut to exact size while providing a smooth clean edge.

Thermal stresses, which are frequently introduced during the machining of PSM-1 if no coolant is provided, were eliminated by allowing water to flow over the surface of the specimen. The coolant flowed onto the specimen from a tube which was attached to a hole in the bottom of a coffee can suspended above the work table.

The last step in machining the specimens was the drilling of the holes, which was done on a standard drill press. The one-fourth inch diameter loading holes at the ends of the specimen were bored using a one-fourth inch end mill to assure uniformity. The two small holes near the root of the notch were drilled directly through the pilot holes in the template, using a number 27 drill bit (0.144 inch diameter) in the drill press. Denatured alcohol sprayed through a syringe acted as a coolant for the specimens during the drilling operations.

Upon completion of the drilling, a sharp knife was used to separate the template from the finished specimen. A fine file was used to eliminate any burrs which resulted from machining and the

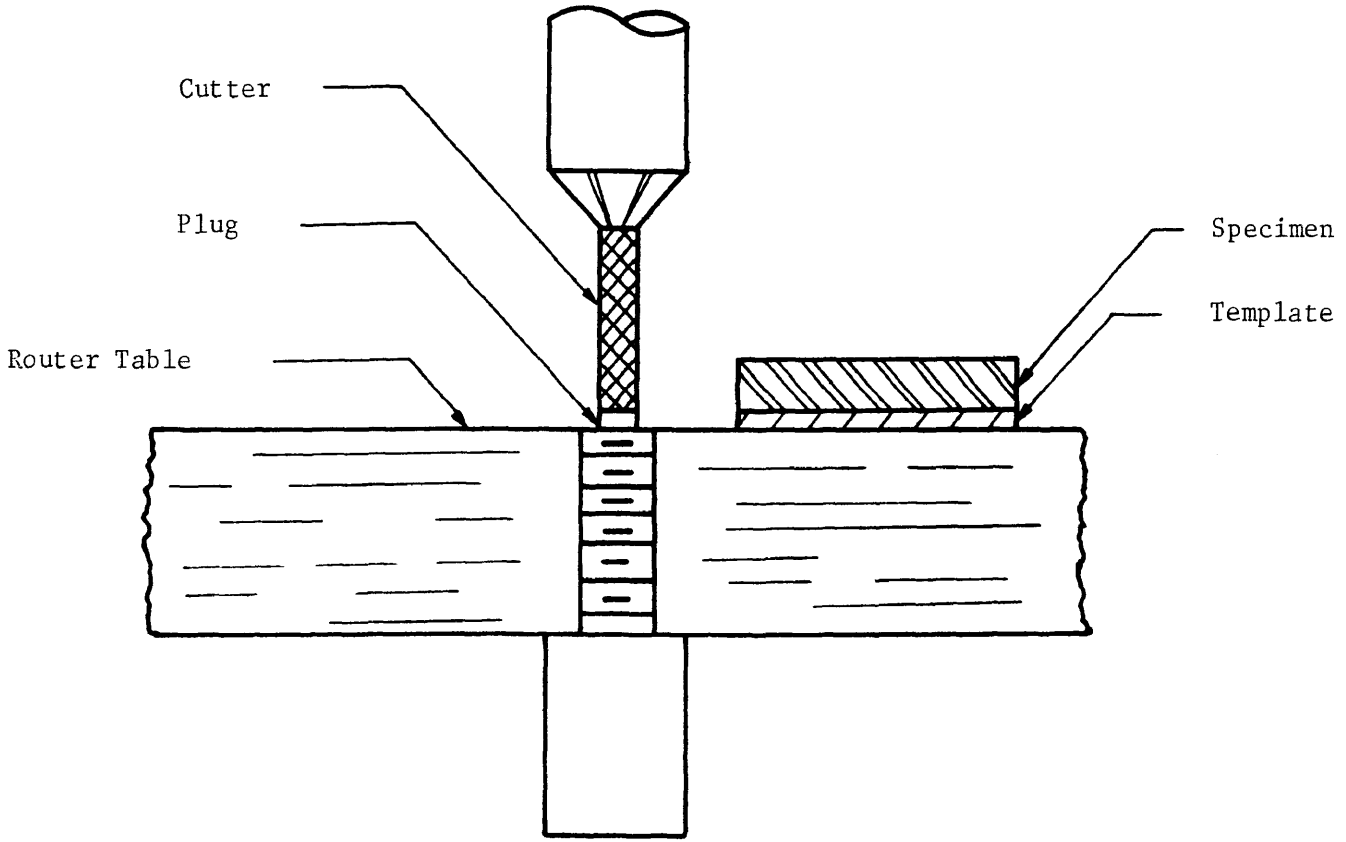

Figure 6. Machining Diagram

entire specimen was cleaned with alcohol to remove any tapemarks or fingerprints. The completed specimen was then ready for testing in the polariscope.

A total of eight specimens were machined, which included a drilled and an undrilled member for each notch depth. The 60% A/W (ratio of notch depth, A, to plate width, W) pair is shown in Figure 5.

V. TEST PROCEDURE

Each specimen was placed in the polariscope and loaded by means of the Dillon testing machine. A new loading fixture was machined for the testing machine in order to position the model directly between the lenses and also to accommodate the specimen design (Figure 7). Test results were compiled for static loads at room temperature. The load for the drilled and undrilled specimens of a given notch depth was held constant for ease of comparison. The load was chosen as that which produced a stress close to the yield stress of the material, but with sufficient image resolution and sharpness for photographic analysis.

The initial step in testing was calibration of the strain gage meter readout. The meter was switched on and allowed to remain for fifteen minutes to permit the components to stabilize. Calibration was performed according to the manufacturers specifications. The polariscope was turned on and the specimen loaded in the testing machine. The fringes were observed and photographed for the dark and light field configurations (Figure 8) of the polariscope in order to determine the integral and half order fringe values. Two photographs were taken of each configuration, a close-up view of the specimen, which was used to study the concentration of fringes at the notch root, and a full view to point out the overall stress distribution.

The close-up photographs were taken with the Nikon F camera attached to the polariscope frame. The 43mm to 86mm zoom lens and bellows were used to provide a 16x magnification of the notch root.

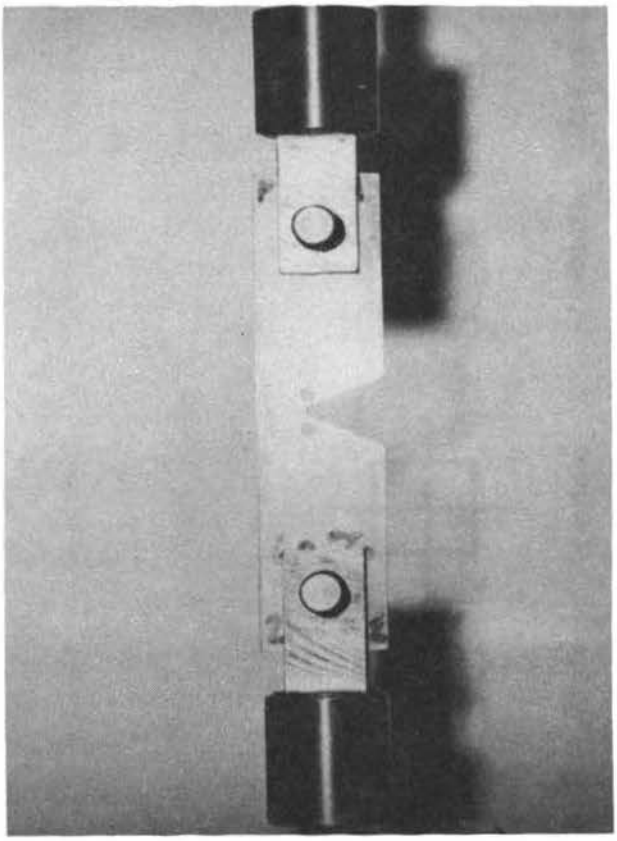

Figure 7. Specimen Loading Fixture

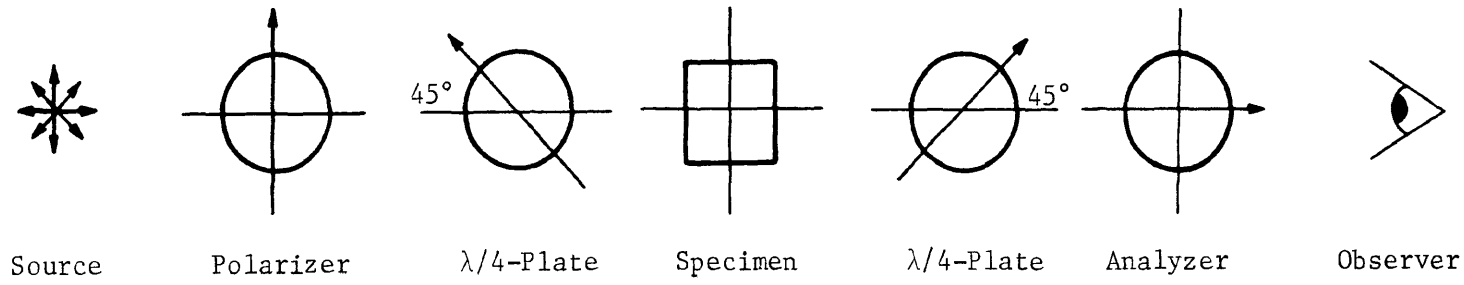

a. Dark Field

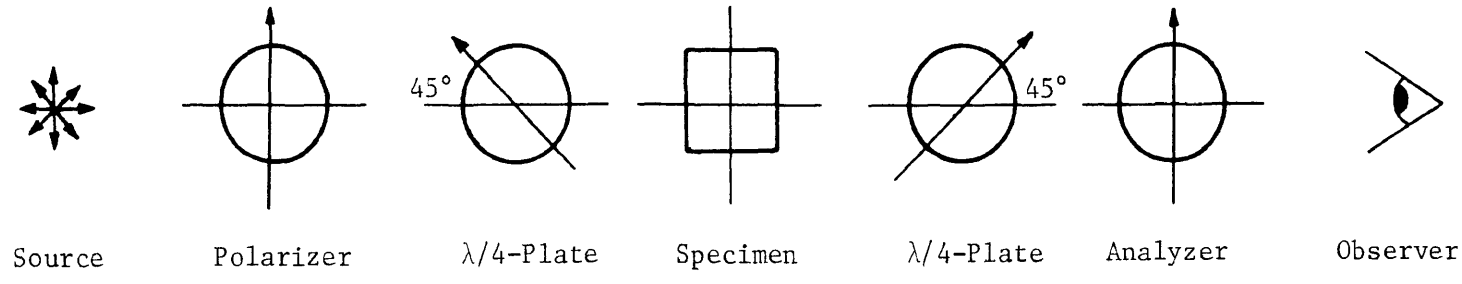

b. Light Field

Figure 8. Circular Polariscope Lens Orientation

The 135mm lens was then substituted for the zoom lens, and the camera was mounted on a tripod for the full image photographs at a distance of thirty inches from the image. Exposures and test loads for all specimens are listed in Table 2.

After all specimens were tested and photographed the negatives were developed (23) and prints were made in the Engineering Mechanics department's darkroom.

TABLE II

Specimen Test Loads and Film Exposures
(Kodak Plus-X Pan Film - 125 ASA)

A/W %	Drilled Holes	Test Load (Pounds)	Close-up Exposures time (sec)	f-stop	Full View Exposures time (sec)	f-stop
20	NO	100	9	4	9	7 1/2
20	YES	100	9	4	9	7 1/2
40	NO	60	9	4	9	7 1/2
40	YES	60	9	4	9	7 1/2
60	NO	20	9	4	9	7 1/2
60	YES	20	9	4	9	7 1/2
80	NO	5	9	4	9	7 1/2
80	YES	5	9	4	9	7 1/2

VI. ANALYSIS AND RESULTS

A. Finite Element Analysis

A finite element study of the notched specimen using Wilson's program (24) provided an analytical comparison for the photoelastic study. The program was run on the IBM 360/50 computer.

The purpose of the program is to determine stresses and deformations within plane or axisymmetric structures of arbitrary shape. Analysis is accomplished by the evaluation of the specimen stiffness matrix according to specified boundary conditions (25). Wilson's method incorporates such variables as displacement, stress boundary condition, concentrated loads, gravity and temperature changes. Nonlinear material properties may also be included using a successive approximation technique.

The initial step in this procedure is to select a finite element representation of the two-dimensional shape of the specimen. The notched specimen used in this analysis is symmetric about the notch, therefore, only one half of the member is needed. The elements and their corresponding nodal points are numbered in sequence beginning with one. Elements were drawn successively smaller as the notch root was approached, because of the high stress gradient present at the root. The specific location of each nodal point along with any load or displacement information which is available is used as input for the program. A complete listing of all input information is provided in Appendix B.

The finite element grids were drawn to simulate the drilled and undrilled specimens (Figures 9, 10, 11). The 60% A/W notched

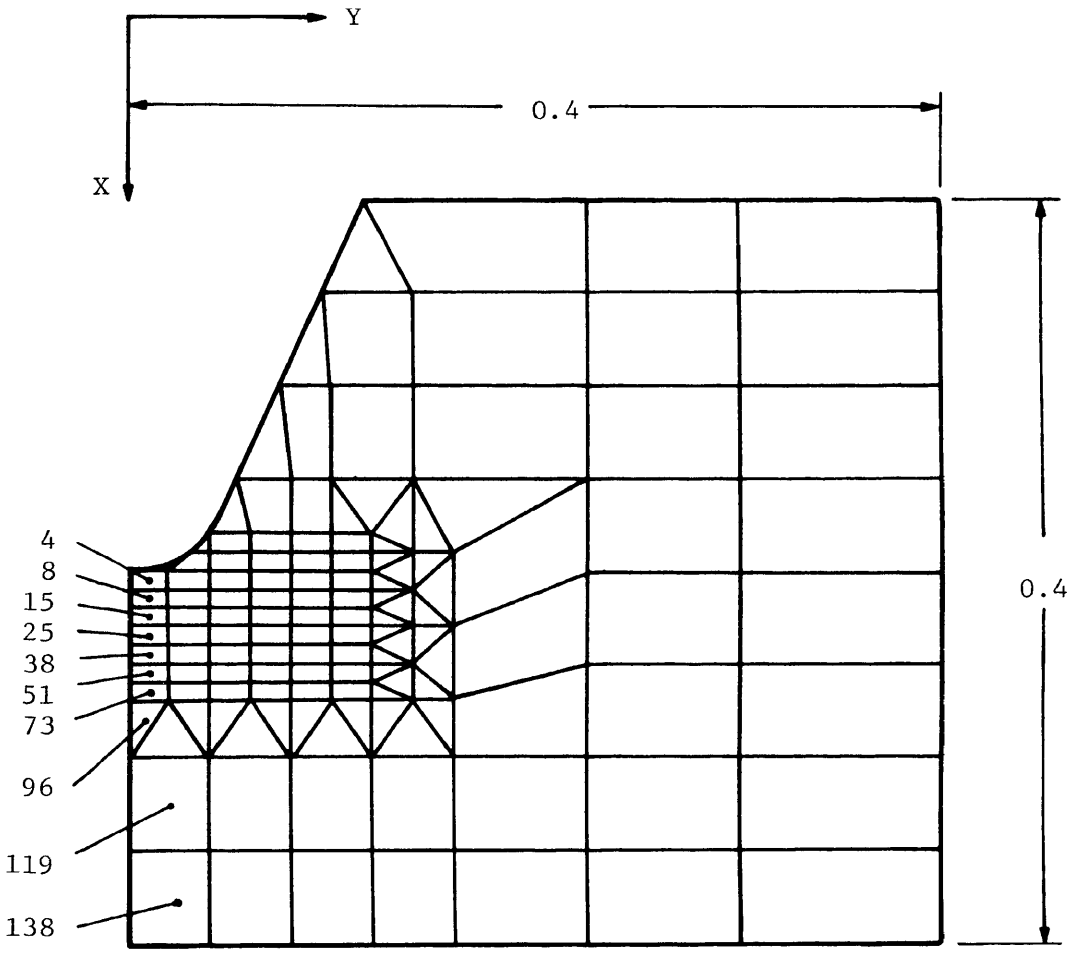

Section A

Figure 9. Finite Element Grid 60% A/W Undrilled
(Scale 10:1)

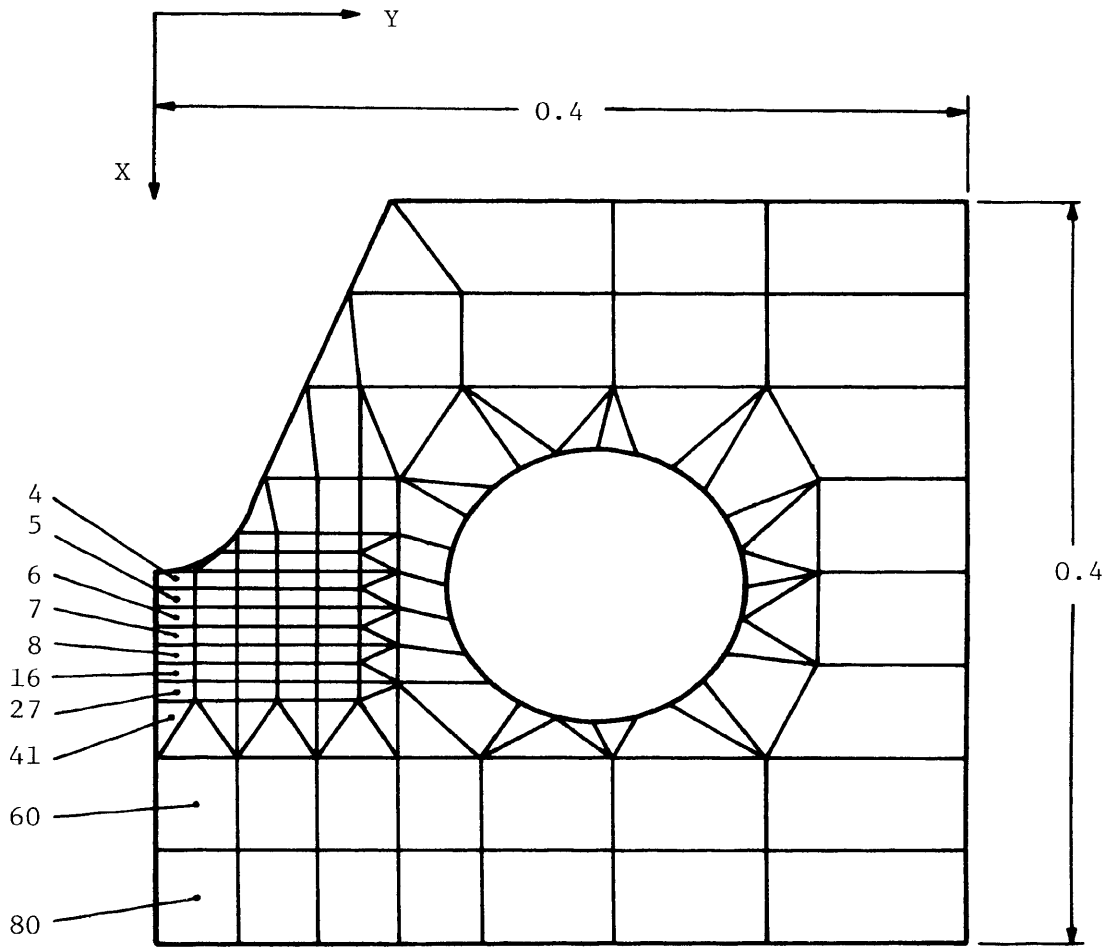

Figure 10. Finite Element Grid 60% A/W Drilled
(Scale 10:1)

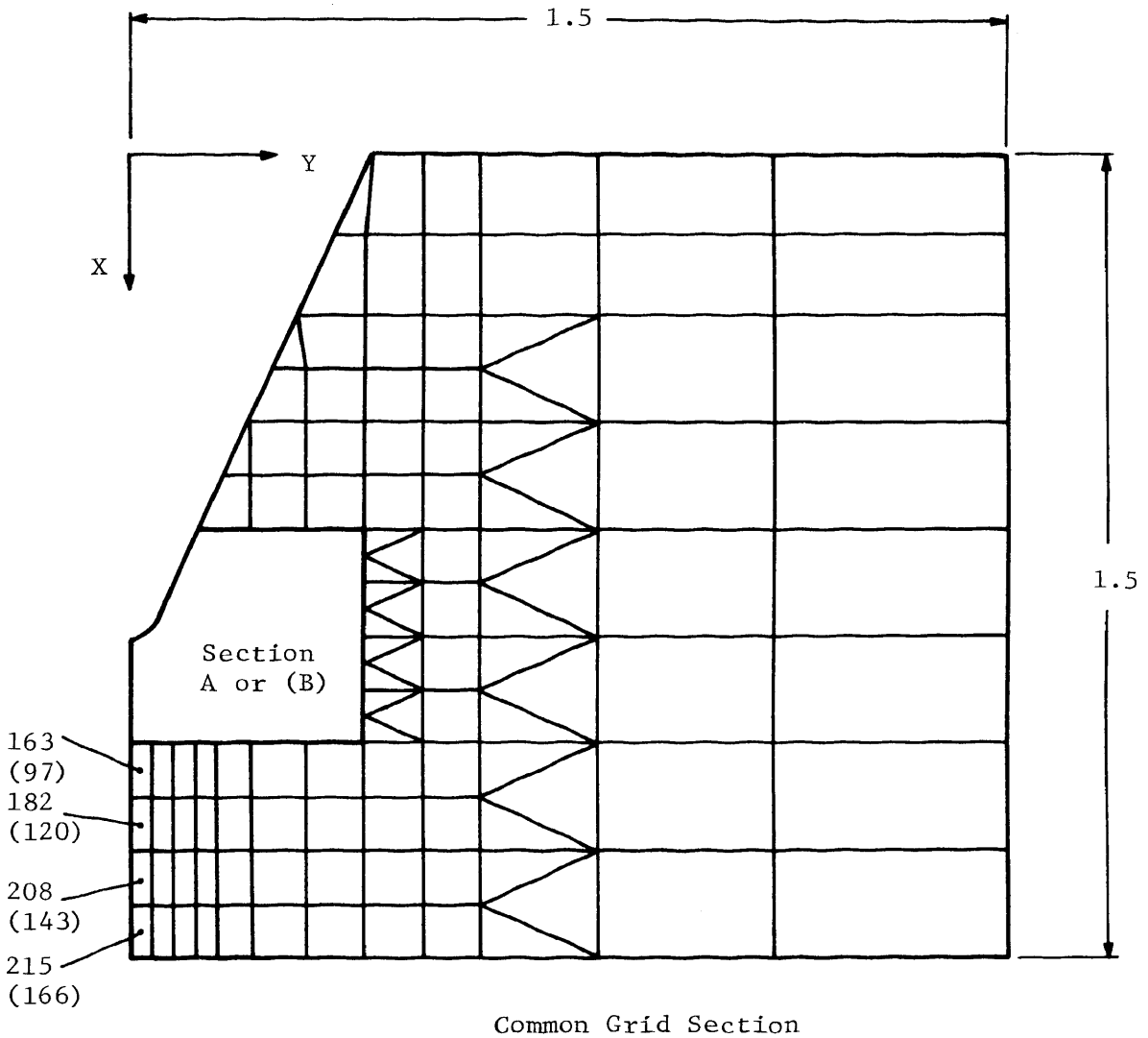

Figure 11. Finite Element Grid 60% A/W Drilled and Undrilled (Scale 3:1)

Note: Numbers referred to above in parentheses are used in conjunction with Section B.

specimens were chosen for this modeling. The actual test load of twenty pounds was used to calculate the input stress based on the gross cross sectional area of the specimen (Appendix B). The principal stress differences (σ_1-σ_2) were found from the computer output for the numbered elements in Figures 9, 10, and 11. The values of (σ_1-σ_2) along with the corresponding locations are listed in Tables III and IV for the 60% A/W notched specimens.

B. Photoelastic Analysis

The photographs of each notch depth (Figures 12, 13, 14, 15) were inspected and calculations were made from the isochromatics (Figure 16) to determine the values of the principal stress differences along the plane of symmetry of the notch according to the formula (26).

$$\sigma_1 - \sigma_2 = Fn/h$$

Actual locations of these fringes were determined by calculating a scale factor for each photograph based on some known dimension in the photograph itself. A detailed procedure of this method is outlined in Appendix C. The values of (σ_1-σ_2) and the respective locations are listed in Tables V through XII for all the notched specimens.

C. Results

A comparison of the numerical and experimental methods of analysis for the 60% A/W notched specimens is presented in Figures 17 and 18. The principal stress difference versus the distance across the notch plane was plotted and compatible results were exhibited for the drilled and undrilled specimens.

TABLE III

Computer Results - 60% A/W - Undrilled

Element Number	Centroid Location (inches)		Stress Difference (psi)
	X	Y	$\sigma_1-\sigma_2$
4	0.905	0.010	1380
8	0.915	0.010	877
15	0.925	0.010	602
25	0.935	0.010	437
38	0.945	0.010	329
51	0.955	0.010	254
73	0.965	0.010	200
96	0.980	0.006	201
119	1.025	0.020	89
138	1.075	0.020	46
163	1.150	0.020	42
182	1.250	0.020	89
208	1.350	0.020	162
225	1.450	0.020	278

TABLE IV

Computer Results - 60% A/W - Drilled

Element Number	Centroid Location (inches)		Stress Difference (psi)
	X	Y	$\sigma_1-\sigma_2$
4	0.905	0.010	1352
5	0.915	0.010	810
6	0.925	0.010	500
7	0.935	0.010	312
8	0.945	0.010	195
16	0.955	0.010	124
27	0.965	0.010	84
41	0.980	0.006	115
60	1.025	0.020	103
80	1.075	0.020	85
97	1.150	0.020	40
120	1.250	0.020	62
143	1.350	0.020	164
166	1.450	0.020	309

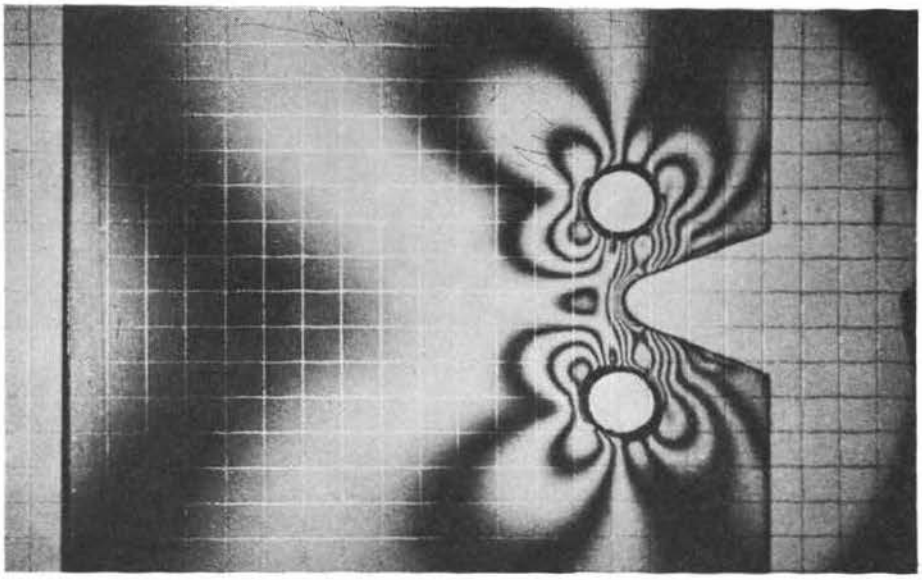

a. Drilled

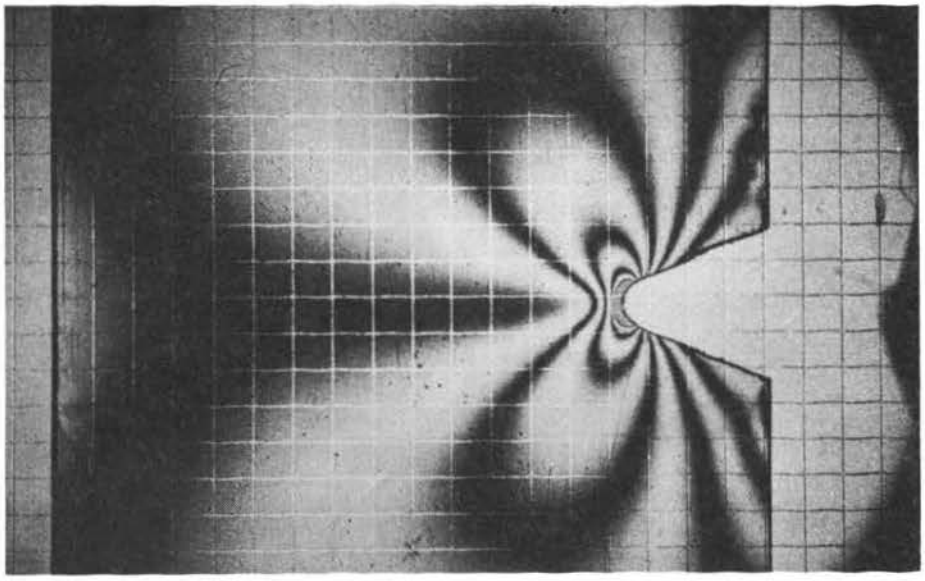

b. Undrilled

Figure 12. 20% A/W SEN Specimen in Tension

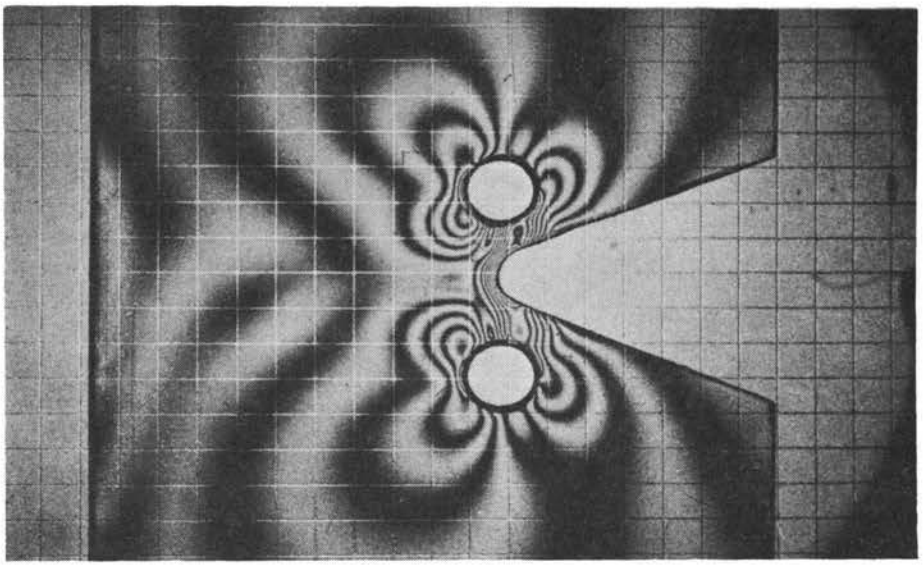

a. Drilled

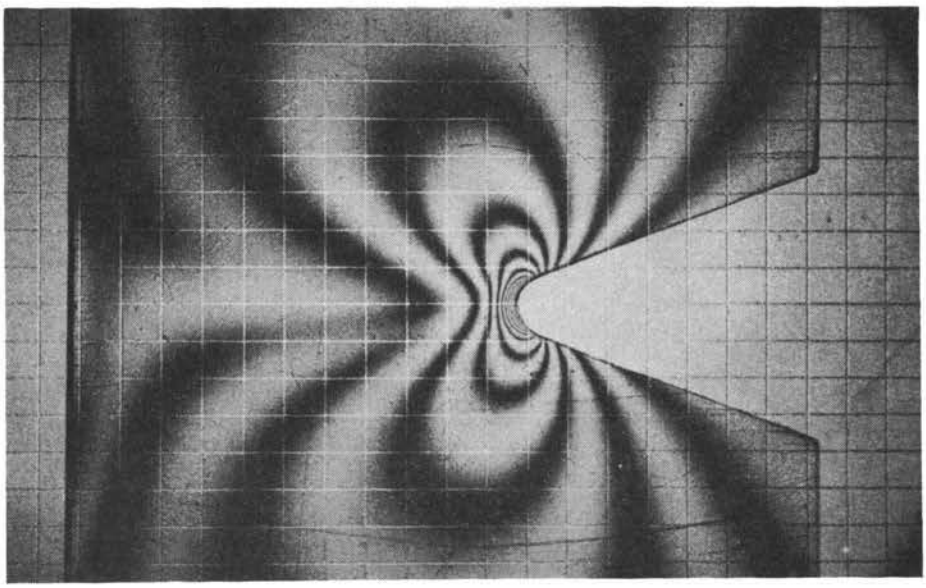

b. Undrilled

Figure 13. 40% A/W SEN Specimen in Tension

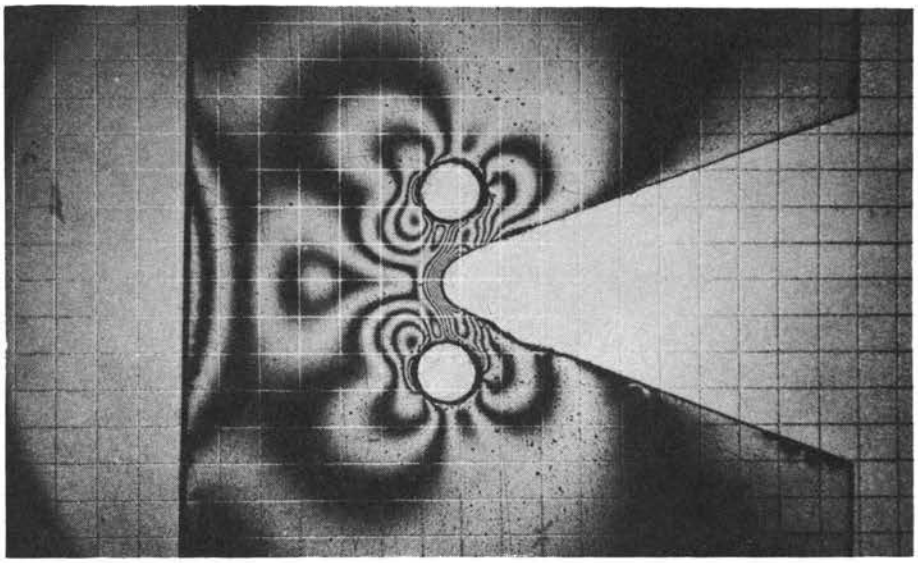

a. Drilled

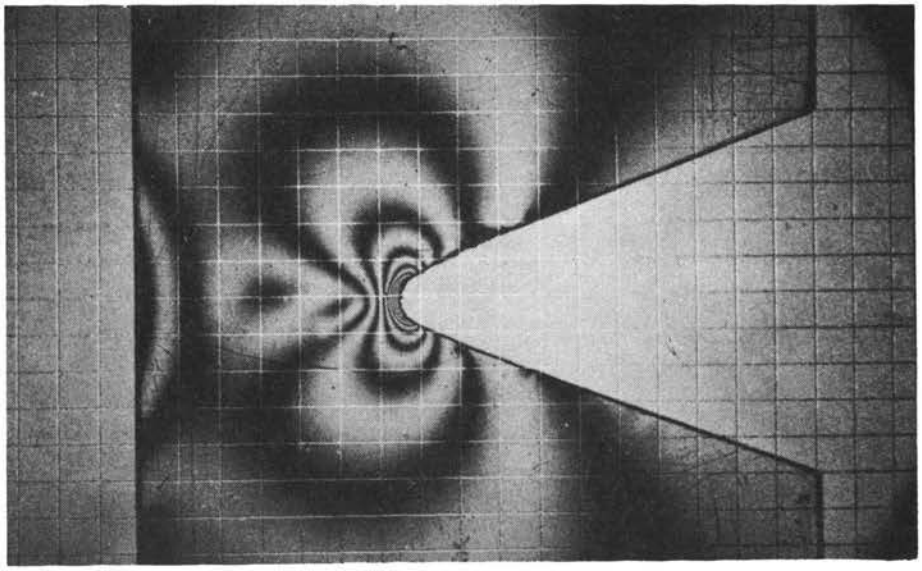

b. Undrilled

Figure 14. 60% A/W SEN Specimen in Tension

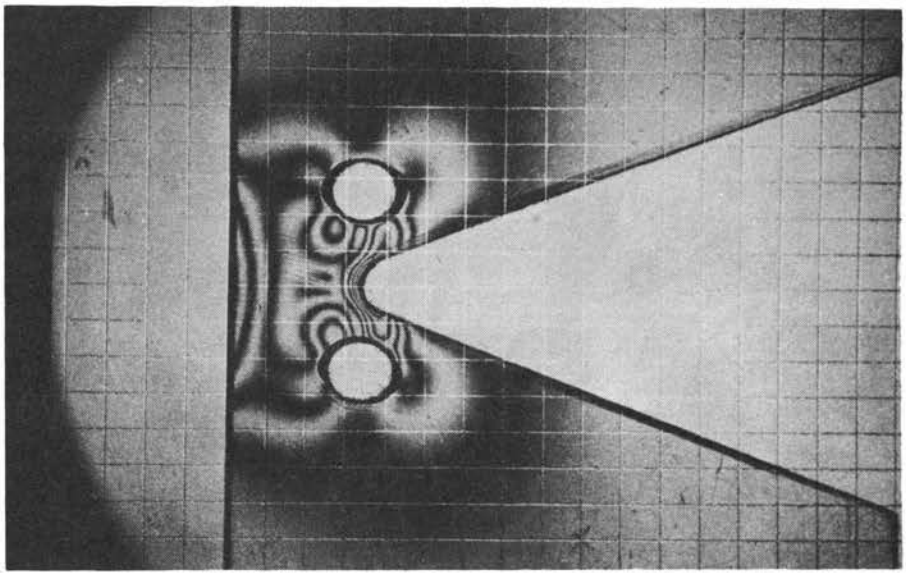

a. Drilled

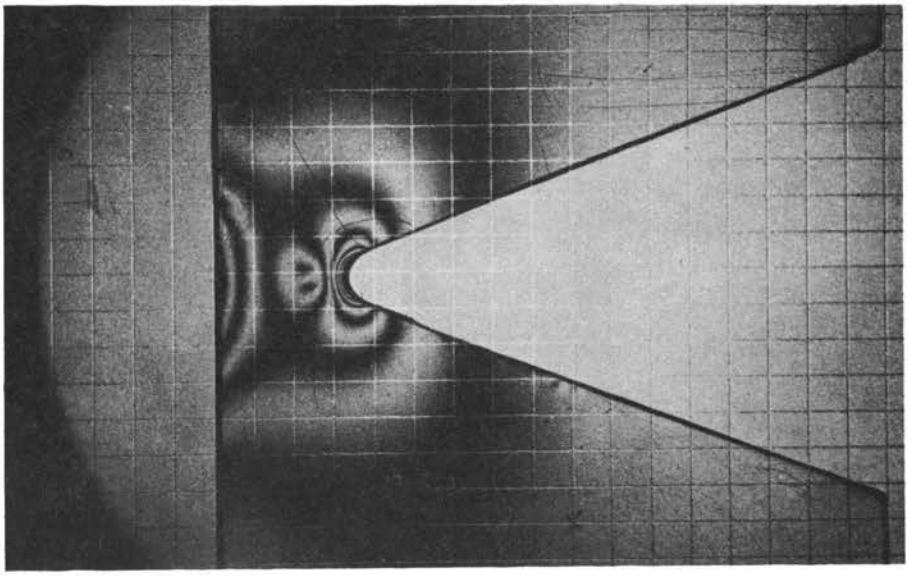

b. Undrilled

Figure 15. 80% A/W SEN Specimen in Tension

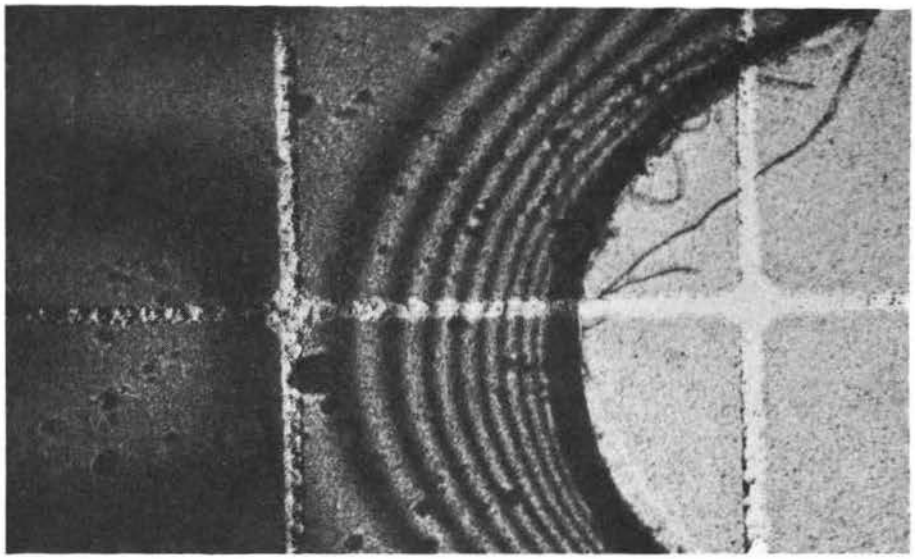

a. Drilled

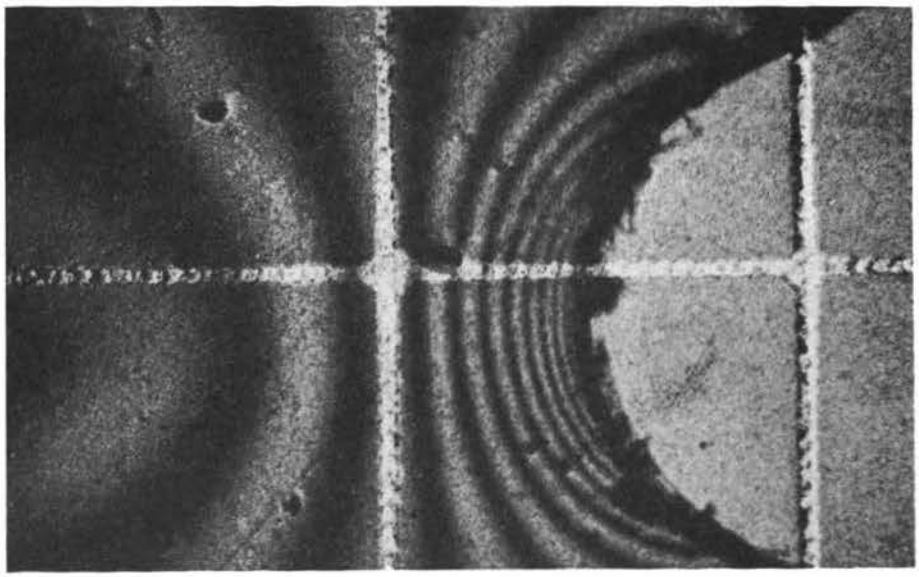

b. Undrilled

Figure 16. Close-up View of 60% A/W SEN Specimen

TABLE V

Experimental Data - 20% A/W - drilled

Fringe Order n	Photo Distance d_p (inches)	Actual Distance d_a (inches)	Total Distance X (inches)	Stress Difference $\sigma_1-\sigma_2$ (psi)
8 1/2	0.000	0.0000	0.3000	1286
8	0.030	0.0017	0.3017	1210
7 1/2	0.050	0.0021	0.3021	1134
7	0.110	0.0045	0.3045	1059
6 1/2	0.130	0.0053	0.3053	983
6	0.200	0.0082	0.3082	907
5 1/2	0.230	0.0094	0.3094	832
5	0.300	0.0123	0.3123	756
4 1/2	0.350	0.0144	0.3144	680
4	0.460	0.0189	0.3189	605
3 1/2	0.510	0.0209	0.3209	529
3	0.650	0.0267	0.3267	453
2 1/2	0.780	0.0320	0.3320	378
2	1.040	0.0426	0.3426	302
1 1/2	1.920	0.0787	0.3787	226
1	2.550	0.0929	1.3929	151
1/2	2.800	1.2000	1.5000	75

TABLE VI

Experimental Data - 20% A/W - Undrilled

Fringe Order n	Photo Distance d_p (inches)	Actual Distance d_a (inches)	Total Distance X (inches)	Stress Difference $\sigma_1-\sigma_2$ (psi)
10 1/2	0.000	0.0000	0.3000	1588
10	0.050	0.0021	0.3021	1512
9 1/2	0.090	0.0038	0.3038	1437
9	0.110	0.0046	0.3046	1361
8 1/2	0.150	0.0063	0.3063	1286
8	0.180	0.0076	0.3076	1210
7 1/2	0.220	0.0093	0.3093	1134
7	0.250	0.0105	0.3105	1059
6 1/2	0.330	0.0139	0.3139	983
6	0.380	0.0160	0.3160	907
5 1/2	0.440	0.0185	0.3185	832
5	0.510	0.0215	0.3215	756
4 1/2	0.600	0.0253	0.3253	680
4	0.730	0.0307	0.3307	605
3 1/2	0.880	0.0370	0.3370	529
3	1.090	0.0459	0.3459	453
2 1/2	1.440	0.0606	0.3606	378
2	2.140	0.0901	0.3901	302
1 1/2	1.750	0.7721	1.0721	226
1	2.660	1.1736	1.4736	151
1/2	2.720	1.2000	1.5000	75

TABLE VII

Experimental Data - 40% A/W - Drilled

Fringe Order n	Photo Distance d_p (inches)	Actual Distance d_a (inches)	Total Distance X (inches)	Stress Difference $\sigma_1-\sigma_2$ (psi)
11 1/2	0.000	0.0000	0.6000	1739
11	0.040	0.0017	0.6017	1664
10 1/2	0.060	0.0025	0.6025	1588
10	0.080	0.0033	0.6033	1512
9 1/2	0.110	0.0046	0.6046	1437
9	0.130	0.0054	0.6054	1361
8 1/2	0.180	0.0075	0.6075	1286
8	0.200	0.0083	0.6083	1210
7 1/2	0.250	0.0104	0.6104	1134
7	0.300	0.0125	0.6125	1059
6 1/2	0.350	0.0146	0.6146	983
6	0.400	0.0166	0.6166	907
5 1/2	0.460	0.0191	0.6191	832
5	0.530	0.0220	0.6220	756
4 1/2	0.610	0.0254	0.6254	680
4	0.680	0.0283	0.6283	605
3 1/2	0.790	0.0329	0.6329	529
3	0.900	0.0374	0.6374	453
2 1/2	1.080	0.0449	0.6449	378
2	1.310	0.0545	0.6545	302
1 1/2	0.680	0.3045	0.9045	226
1	0.900	0.4030	1.0030	151
1/2	1.600	0.7165	1.3165	75
1	1.860	0.8329	1.4329	151

TABLE VIII

Experimental Data - 40% A/W - Undrilled

Fringe Order n	Photo Distance d_p (inches)	Actual Distance d_a (inches)	Total Distance X (inches)	Stress Difference $\sigma_1-\sigma_2$ (psi)
11 1/2	0.000	0.0000	0.6000	1739
11	0.050	0.0020	0.6020	1664
10 1/2	0.070	0.0028	0.6028	1588
10	0.110	0.0045	0.6045	1512
9 1/2	0.140	0.0057	0.6057	1437
9	0.190	0.0077	0.6077	1361
8 1/2	0.230	0.0093	0.6093	1286
8	0.270	0.0110	0.6110	1210
7 1/2	0.320	0.0130	0.6130	1134
7	0.380	0.0154	0.6154	1059
6 1/2	0.440	0.0179	0.6179	983
6	0.520	0.0211	0.6211	907
5 1/2	0.600	0.0244	0.6244	832
5	0.700	0.0284	0.6284	756
4 1/2	0.840	0.0341	0.6341	680
4	0.980	0.0398	0.6398	605
3 1/2	1.200	0.0487	0.6487	529
3	1.500	0.0609	0.6609	453
2 1/2	1.950	0.0792	0.6792	378
2	2.800	0.1137	0.7137	302
1 1/2	0.450	0.1891	0.7891	226
1	1.300	0.5463	1.1463	151
1/2	1.950	0.8194	1.4194	75
1	2.060	0.8656	1.4656	151

TABLE IX

Experimental Data - 60% A/W - Drilled

Fringe Order n	Photo Distance d_p (inches)	Actual Distance d_a (inches)	Total Distance X (inches)	Stress Difference $\sigma_1-\sigma_2$ (psi)
10 1/2	0.000	0.0000	0.9000	1588
10	0.030	0.0013	0.9013	1512
9 1/2	0.050	0.0022	0.9022	1437
9	0.090	0.0040	0.9040	1361
8 1/2	0.130	0.0057	0.9057	1286
8	0.160	0.0071	0.9071	1210
7 1/2	0.200	0.0088	0.9088	1134
7	0.240	0.0106	0.9106	1059
6 1/2	0.280	0.0124	0.9124	983
6	0.340	0.0150	0.9150	907
5 1/2	0.380	0.0168	0.9168	832
5	0.460	0.0203	0.9203	756
4 1/2	0.500	0.0221	0.9221	680
4	0.600	0.0265	0.9265	605
3 1/2	0.680	0.0300	0.9300	529
3	0.800	0.0353	0.9353	453
2 1/2	0.900	0.0398	0.9398	378
2	1.100	0.0486	0.9486	302
1 1/2	1.300	0.0574	0.9574	226
1	0.180	0.0823	0.9823	151
1/2	0.450	0.2058	1.1058	75
1/2	0.750	0.3430	1.2430	75
1	0.860	0.3933	1.2933	151
1 1/2	0.980	0.4482	1.3482	226
2	1.060	0.4847	1.3847	302
2 1/2	1.150	0.5259	1.4259	378

TABLE X

Experimental Data - 60% A/W - Undrilled

Fringe Order n	Photo Distance d_p (inches)	Actual Distance d_a (inches)	Total Distance X (inches)	Stress Difference $\sigma_1-\sigma_2$ (psi)
11	0.000	0.0000	0.9000	1664
10 1/2	0.050	0.0021	0.9021	1588
10	0.075	0.0032	0.9032	1512
9 1/2	0.100	0.0043	0.9043	1437
9	0.140	0.0060	0.9060	1361
8 1/2	0.175	0.0074	0.9074	1286
8	0.200	0.0085	0.9085	1210
7 1/2	0.260	0.0111	0.9111	1134
7	0.290	0.0123	0.9123	1059
6 1/2	0.350	0.0149	0.9149	983
6	0.400	0.0170	0.9170	907
5 1/2	0.460	0.0196	0.9196	832
5	0.525	0.0223	0.9223	756
4 1/2	0.610	0.0259	0.9259	680
4	0.700	0.0298	0.9298	605
3 1/2	0.800	0.0340	0.9340	529
3	0.925	0.0393	0.9393	453
2 1/2	0.120	0.0545	0.9545	378
2	0.140	0.0636	0.9636	302
1 1/2	0.160	0.0727	0.9727	226
1	0.350	0.1591	1.0591	151
1/2	0.650	0.2954	1.1954	75
1	0.850	0.3863	1.2863	151
1 1/2	1.025	0.4659	1.3659	226
2	1.140	0.5181	1.4181	302
2 1/2	1.225	0.5568	1.4568	378

TABLE XI

Experimental Data - 80% A/W - Drilled

Fringe Order n	Photo Distance d_p (inches)	Actual Distance d_a (inches)	Total Distance X (inches)	Stress Difference $\sigma_1-\sigma_2$ (psi)
6	0.000	0.0000	1.2000	907
5 1/2	0.050	0.0021	1.2021	832
5	0.100	0.0042	1.2042	756
4 1/2	0.140	0.0059	1.2059	680
4	0.230	0.0098	1.2098	605
3 1/2	0.290	0.0123	1.2123	529
3	0.410	0.0174	1.2174	453
2 1/2	0.480	0.0204	1.2204	378
2	0.640	0.0271	1.2271	302
1 1/2	0.810	0.0343	1.2343	226
1	1.110	0.0471	1.2471	151
1/2	1.630	0.0691	1.2691	75
1/2	0.280	0.1273	1.3273	75
1	0.310	0.1409	1.3409	151
1 1/2	0.420	0.1909	1.3909	226
2	0.480	0.2182	1.4182	302
2 1/2	0.530	0.2409	1.4409	378
3	0.560	0.2545	1.4545	453
3 1/2	0.620	0.2818	1.4818	529

TABLE XII

Experimental Data - 80% A/W - Undrilled

Fringe Order n	Photo Distance d_p (inches)	Actual Distance d_a (inches)	Total Distance X (inches)	Stress Difference $\sigma_1-\sigma_2$ (psi)
6	0.000	0.0000	1.2000	907
5 1/2	0.050	0.0021	1.2021	832
5	0.125	0.0053	1.2053	756
4 1/2	0.175	0.0074	1.2074	680
4	0.250	0.0105	1.2105	605
3 1/2	0.325	0.0137	1.2137	529
3	0.425	0.0169	1.2169	453
2 1/2	0.560	0.0235	1.2235	378
2	0.725	0.0305	1.2305	302
1 1/2	0.940	0.0395	1.2395	226
1	1.250	0.0525	1.2525	151
1/2	2.050	0.0861	1.2861	75
1	0.300	0.1385	1.3385	151
1 1/2	0.400	0.1846	1.3846	226
2	0.425	0.1961	1.3961	302
2 1/2	0.525	0.2423	1.4423	378
3	0.540	0.2492	1.4492	453
3 1/2	0.625	0.2884	1.4884	529

Experimental data for the 60% A/W drilled and undrilled specimens is plotted in Figure 19 and the corresponding numerical data is presented in Figure 20.

Data from the experimental studies of the 20%, 40%, and 80% A/W notched specimens is compared in Figures 21 through 23.

All plots exhibited very close agreement with each other for all notch sizes.

The elastic stress concentration factor (K_σ) for each specimen was calculated according to the formula (27)

$$K_\sigma = \sigma_{max}/\sigma_{nom}$$

where σ_{max} is the maximum stress at the notch root, and σ_{nom} is the stress acting across the gross cross-section. Values from these calculations for the 60% A/W notched specimens are listed in Table XIII, along with the percentage of deviation based on the undrilled sample.

The calculated values of the elastic stress concentration factors of all specimens tested are presented in Table XIV.

TABLE XIII
K_σ Values for 60% A/W

Method	Drilled	Undrilled	% Deviation
Experimental	29.79	31.22	4.6
Numerical	25.40	25.90	1.9

The 19% deviation of the drilled and undrilled 20% A/W specimens from Table XIV was found to have been caused by the template used to machine the model. The template was accurately measured and the

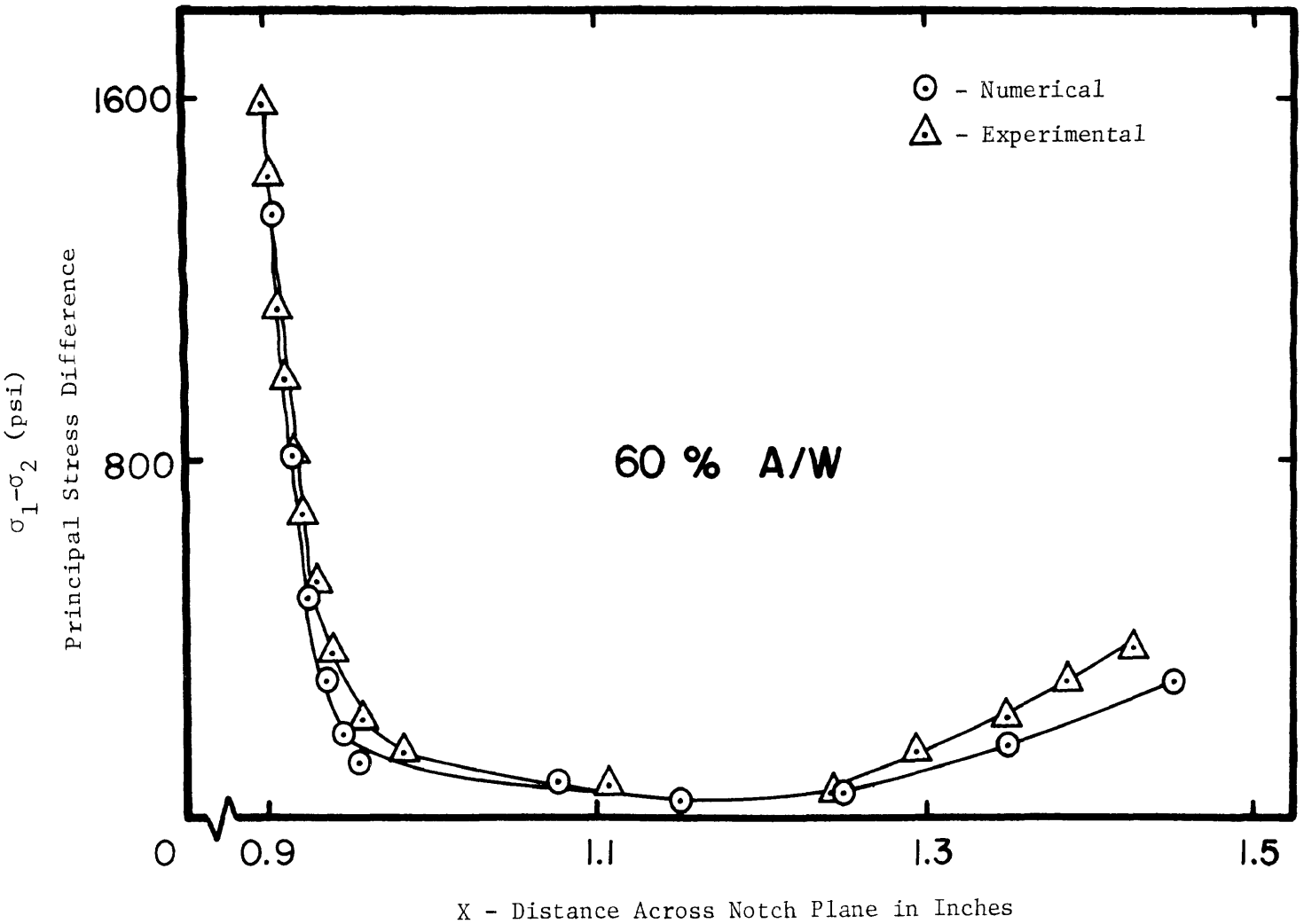

Figure 17. Stress Distribution for 60% A/W (Drilled)

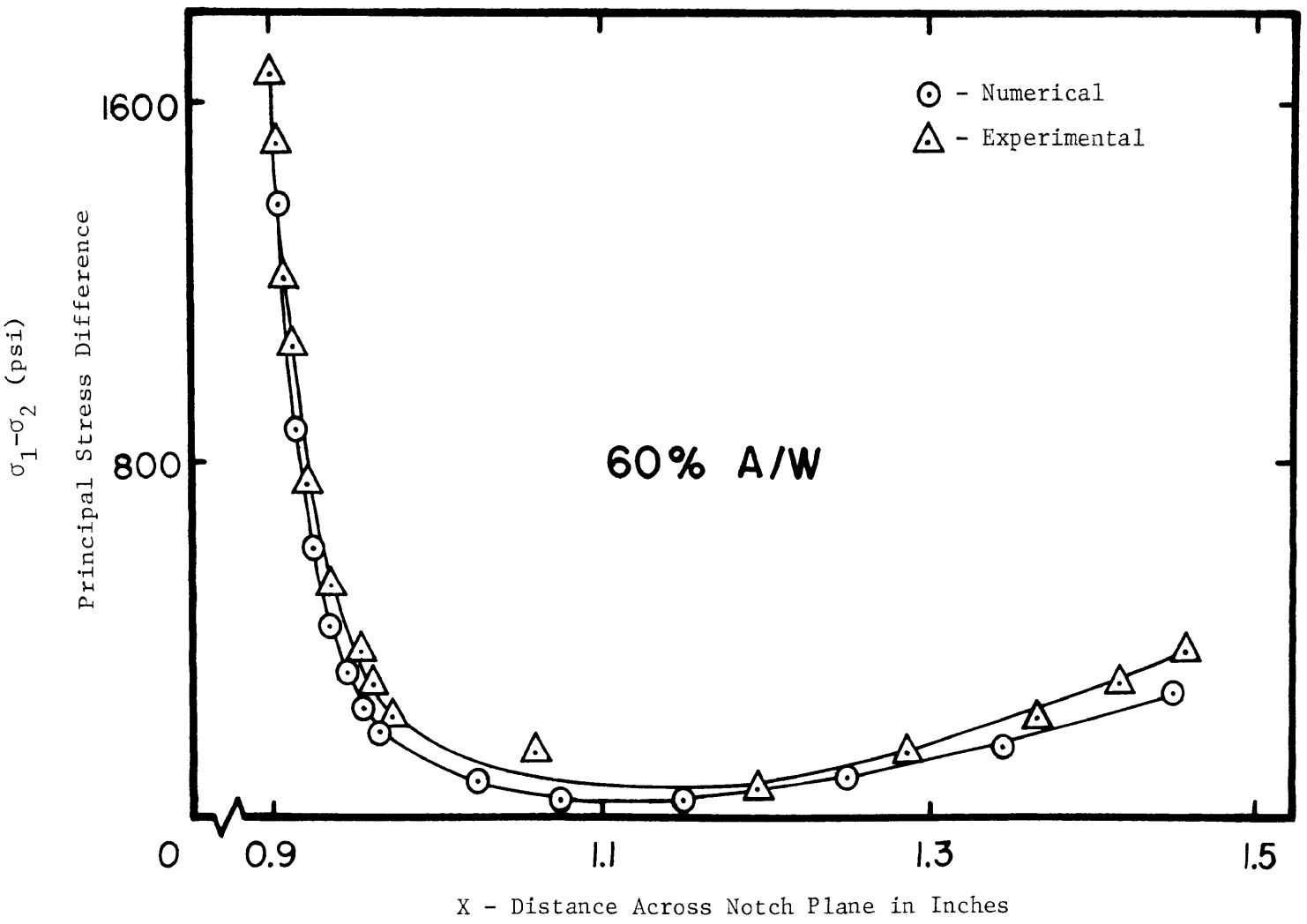

Figure 18. Stress Distribution for 60% A/W (Undrilled)

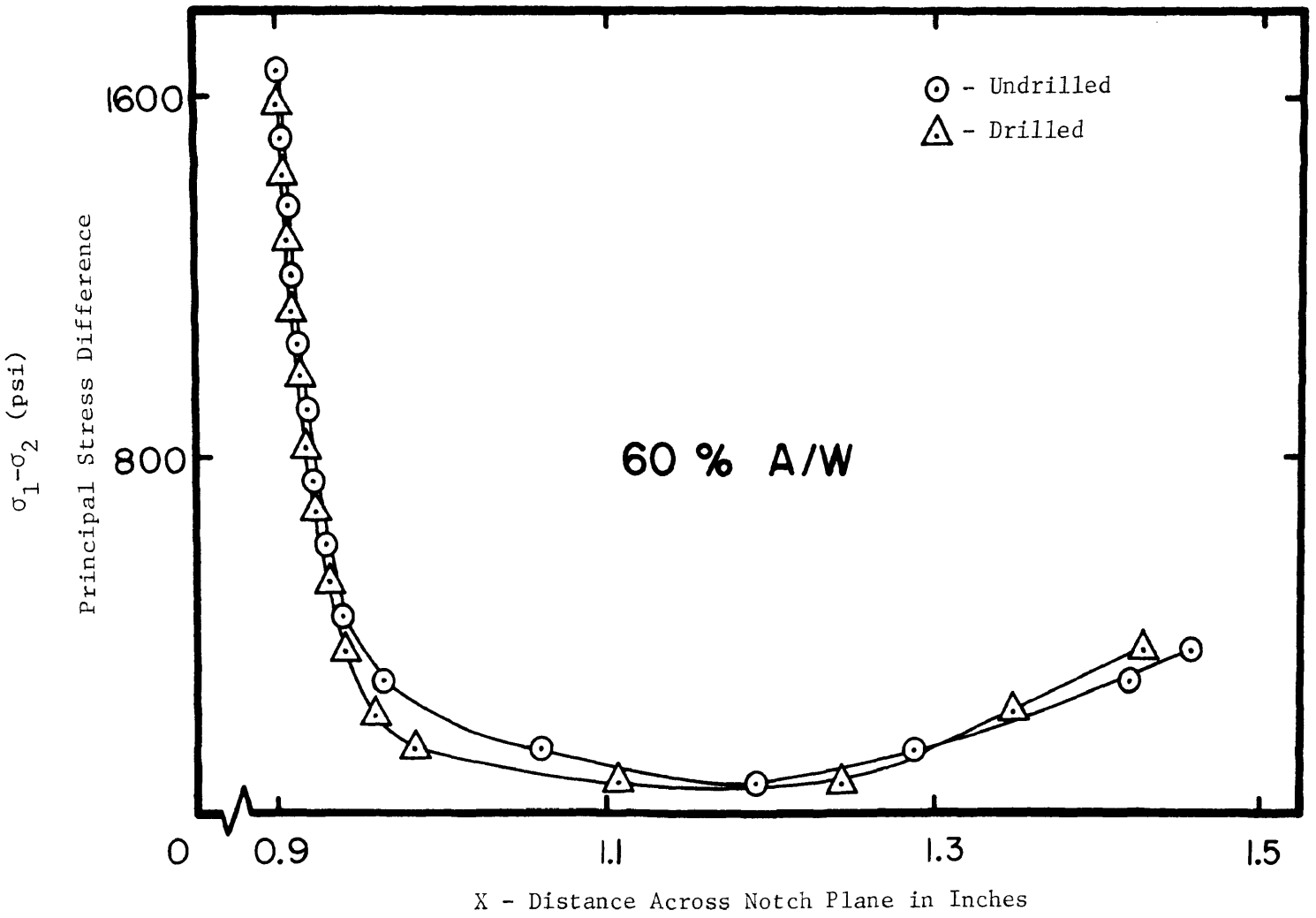

Figure 19. Stress Distribution for 60% A/W (Experimental)

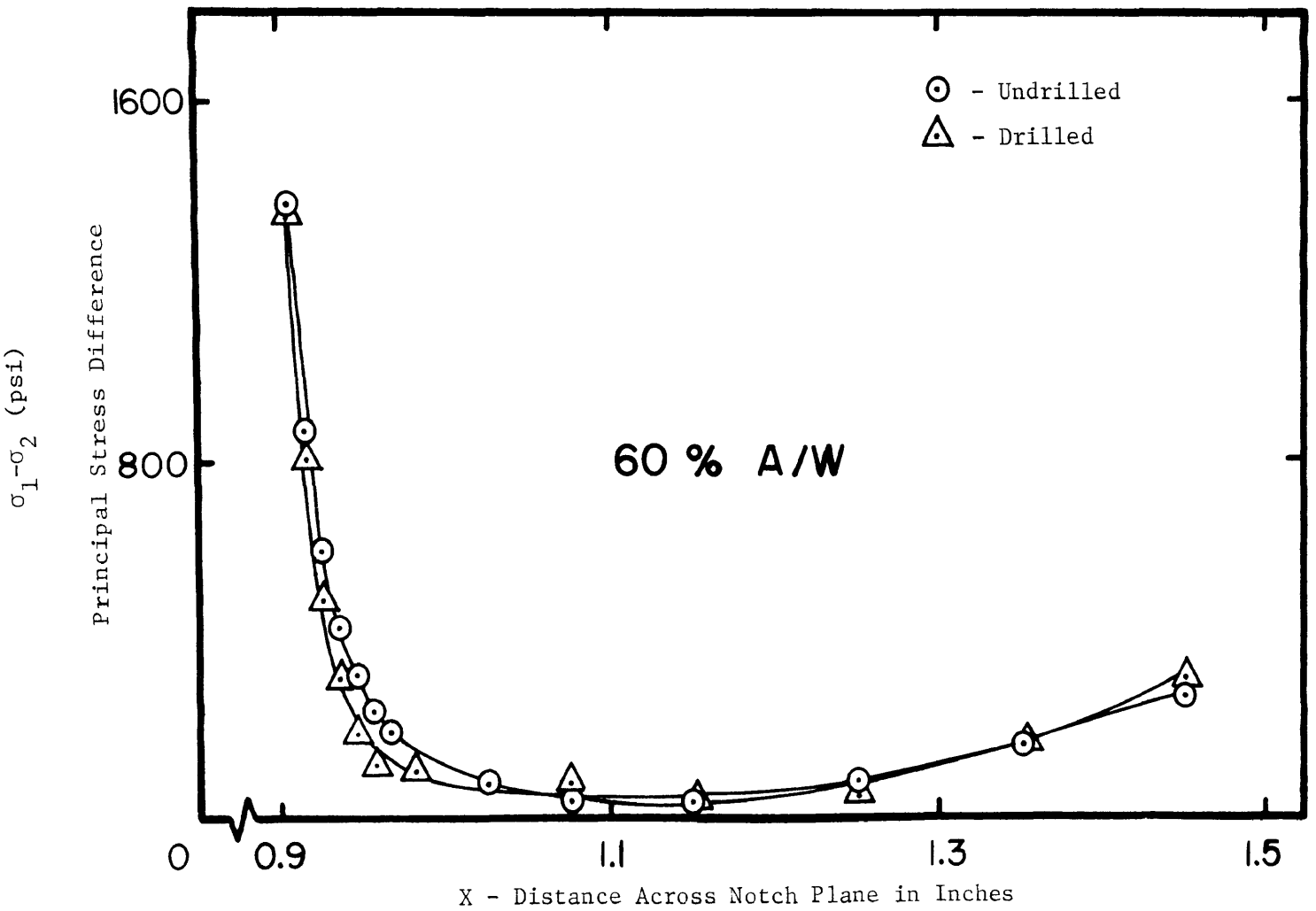

Figure 20. Stress Distribution for 60% A/W (Numerical)

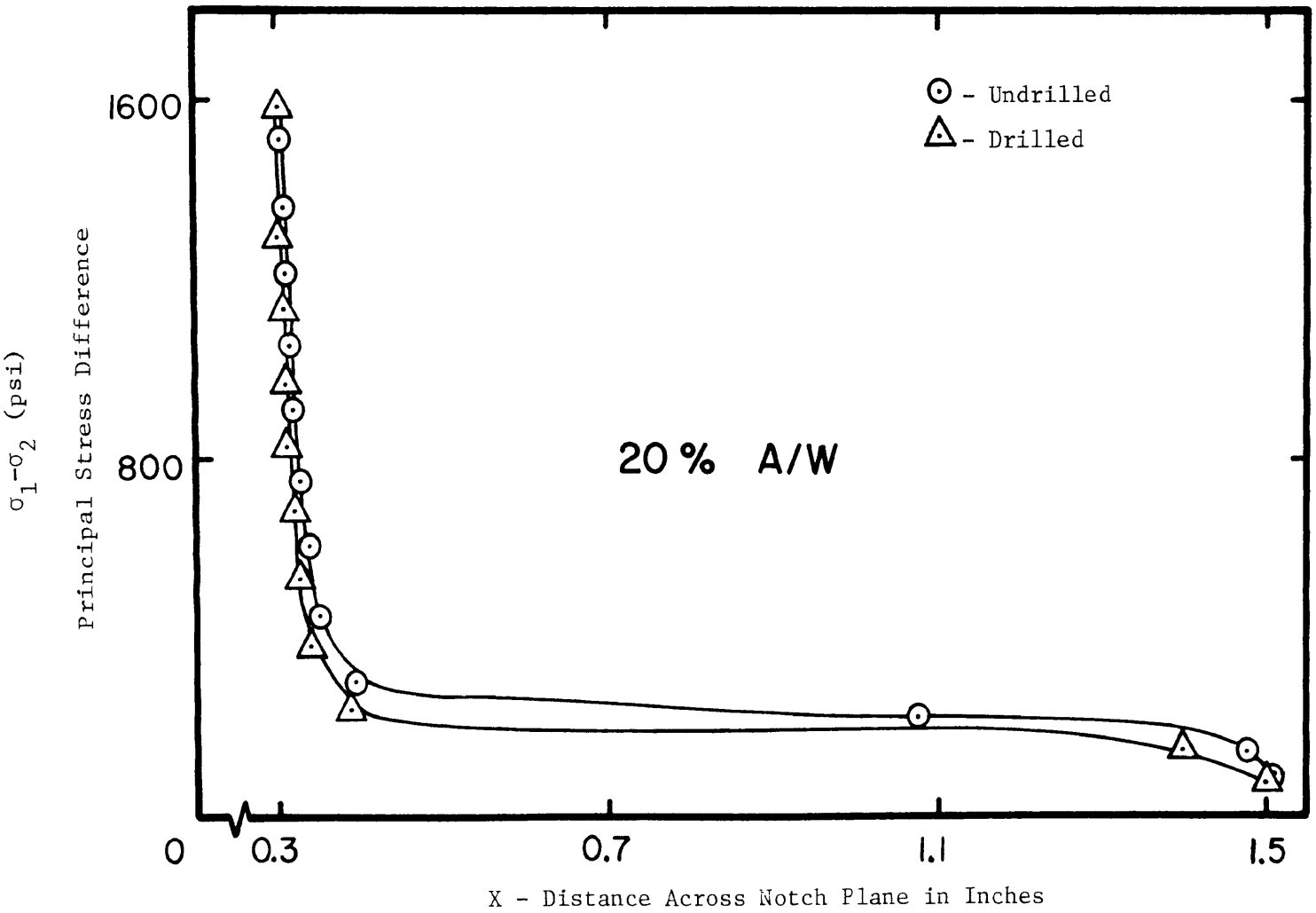

Figure 21. Stress Distribution for 20% A/W

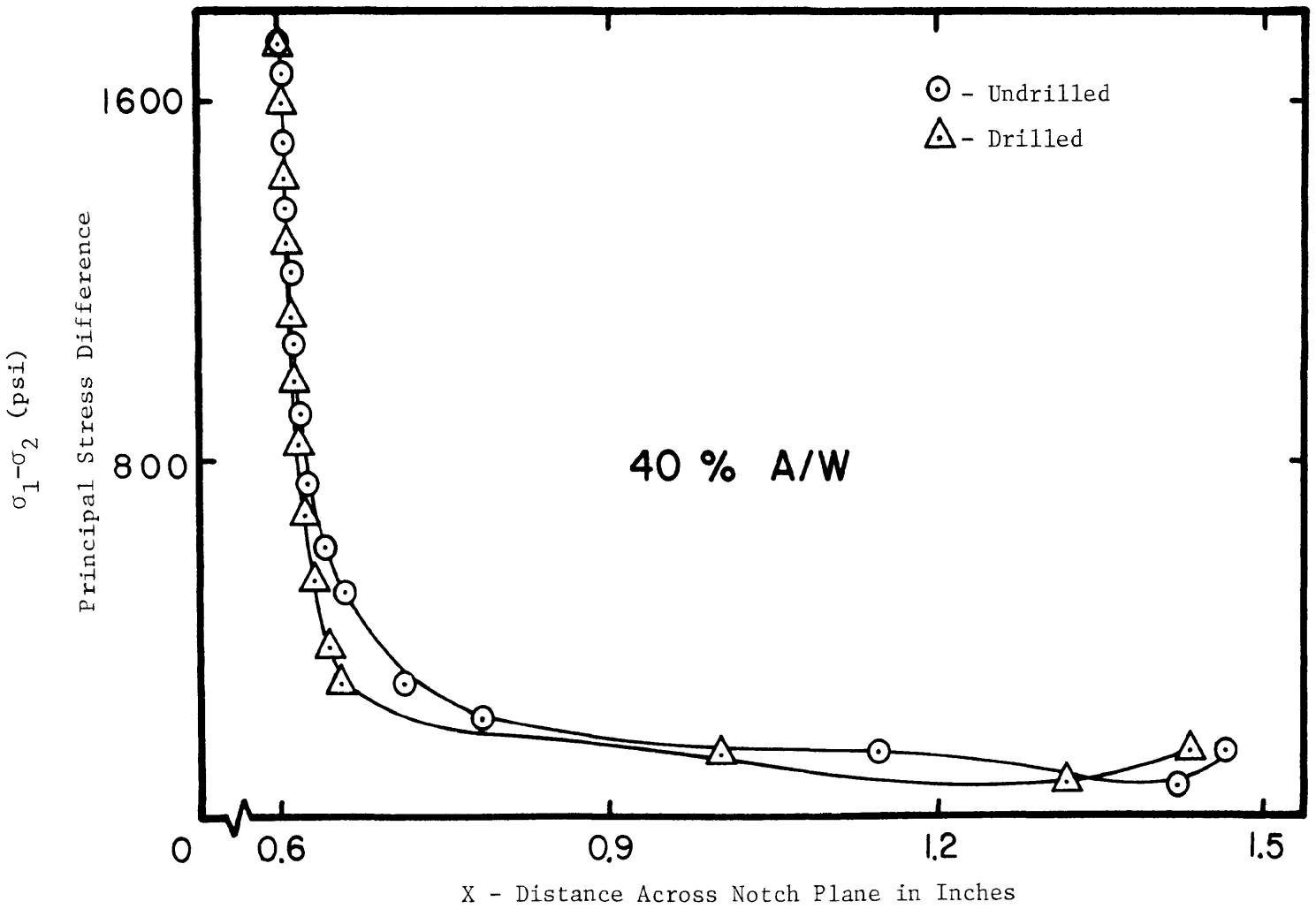

Figure 22. Stress Distribution for 40% A/W

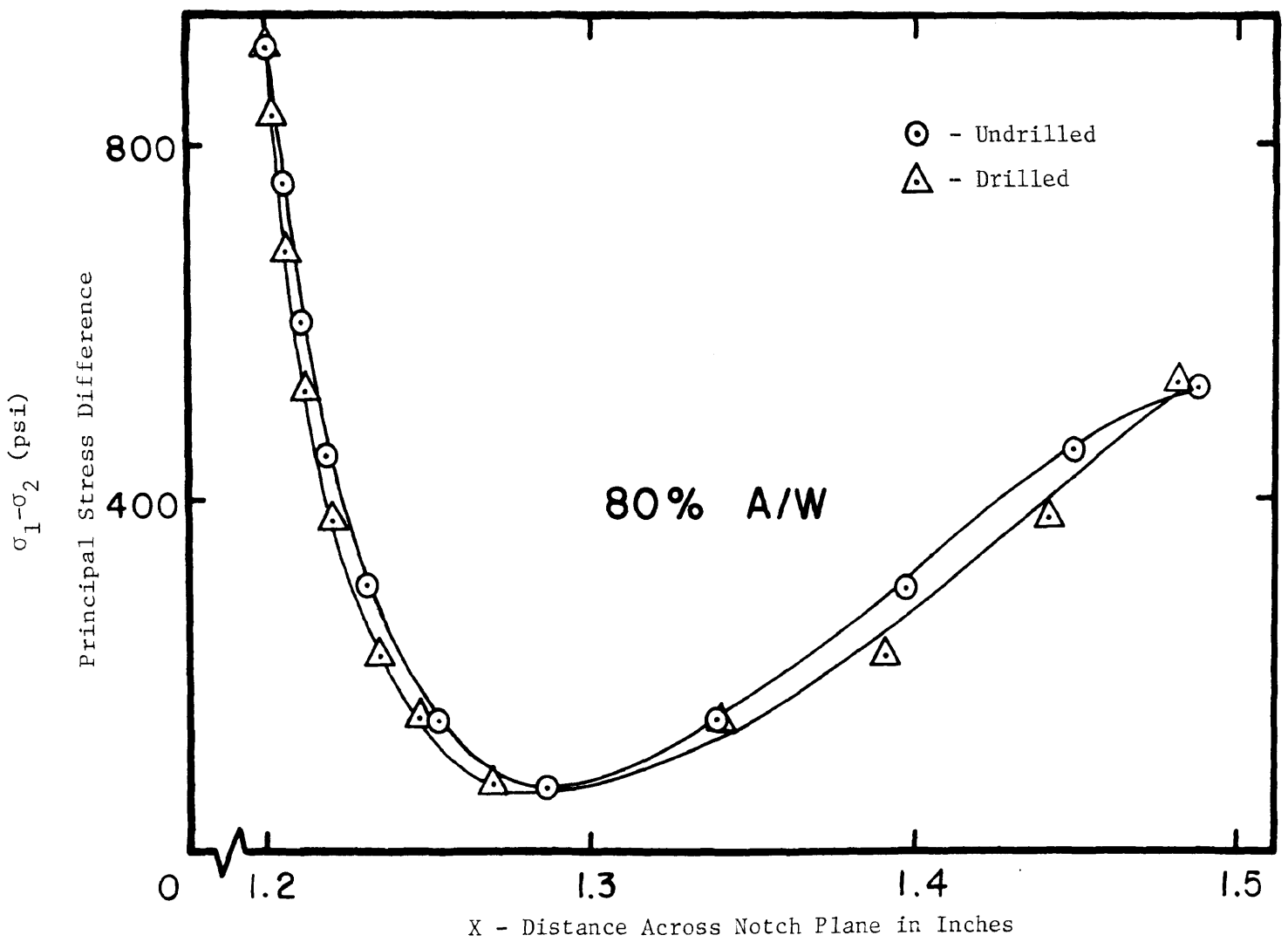

Figure 23. Stress Distribution for 80% A/W

TABLE XIV

K_σ Values for All Notched Specimens

Specimen A/W	σ_{max} psi	P_{nom} lbs	A_{nom} in^2	σ_{nom} psi	K_σ -	Deviation %
20% undrilled	1588	100	0.375	266.7	5.95	-
20% drilled	1286	100	0.375	266.7	4.82	19.0
40% undrilled	1739	60	0.375	160.0	10.87	-
40% drilled	1739	60	0.375	160.0	10.87	0.0
60% undrilled	1664	20	0.375	53.3	31.22	-
60% drilled	1588	20	0.375	53.3	29.79	4.6
80% undrilled	907	5	0.375	13.3	68.19	-
80% drilled	907	5	0.375	13.3	68.19	0.0

drilled holes were found to have been misaligned with respect to the notch root. All other results indicated a percent deviation of less than five which is acceptable from an experimental standpoint.

VII. CONCLUSION

Results established from the notched specimen analysis lead to the following conclusions.

1) No significant increase in the elastic stress concentration factor (K_σ) occurs when proper alignment of the drilled holes is accomplished.
2) Both experimental and numerical results of the tension test performed in this study compare almost identically with the results of the bending test presented by Tetelman and Rau (5) (Figure 24), therefore verifying the method of analysis.
3) The finite element method of stress analysis is an accurate means of determining stresses around a notch, without complex mathematical formulation.
4) Field use of this method of hole drilling would be difficult to accomplish unless the proper equipment were available to locate the exact position of the holes. Misalignment by only a few thousandths of an inch, as evidenced by the 20% A/W specimen, tends to increase the elastic stress concentration factor. Tetelman and Rau (1) have demonstrated this misalignment to have an undesirable effect on the fracture toughness.

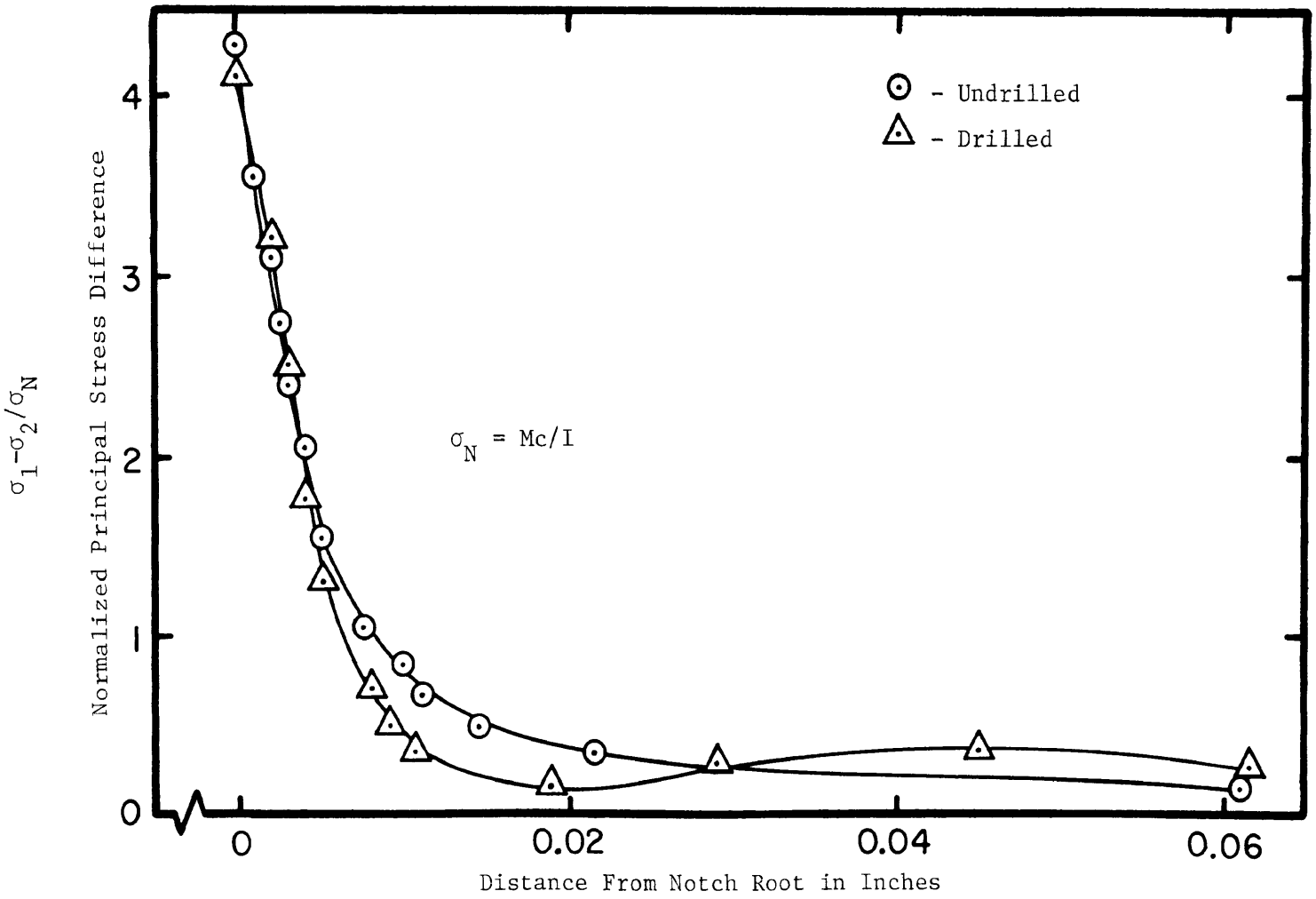

Figure 24. Experimental Results for Charpy V-Notch in Bending (5)

BIBLIOGRAPHY

1. Tetelman, A.S. and Rau, C.A., Jr., "The Effect of Small Drilled Holes on the Notch Toughness of Iron Base Alloys," Proceedings of the International Conference on Fracture, 2, 691 (1965).

2. Tetelman, A.S. and Rau, C.A., Jr., "Strength Through Holes," New Scientist, 4, 103 (1966).

3. Dieter, G.E., Jr., Mechanical Metallurgy, New York: McGraw Hill Book Company, 46 (1961).

4. Rau, C.A., Jr., "The Effect of Drilled Holes on Notch Toughness," Ph.D. Thesis, Stanford University (1967).

5. Tetelman, A.S. and Rau, C.A., Jr., "Effect of Two Drilled Holes on the Elastic and Elastic-Plastic Strain Distribution Around a Charpy V-Notch," Experimental Mechanics, 10, 362 (1970).

6. Griffith, A.A., "The Phenomena of Rupture and Flow in Solids," Philosophical Transactions of the Royal Society, A221, 163 (1920).

7. Griffith, A.A., "Theory of Rupture," Proceedings, First International Congress for Applied Mechanics, Delft, 55 (1924).

8. Orowan, E., "Fracture and Strength of Solids," Reports on Progress in Physics, XII, 185 (1948).

9. Orowan, E. and Felbeck, D.K., "Experiments on Brittle Fracture of Steel Plates," Welding Journal, 34, 570s (1955).

10. Orowan, E., "Notch Brittleness and the Strength of Metals," Transactions, Institution of Engineers and Shipbuilders in Scotland, 89, 165 (1945).

11. Irwin, G.R., "Fracture," Encyclopedia of Physics, VI, Heidelberg: Springer (1958).

12. Zener, C., "The Micro-Mechanism of Fracture," Transactions of the American Society for Metals, 40A, 3 (1948).

13. Stroh, A.N., "The Formation of Cracks as a Result of Plastic Flow," Proceedings, Royal Society of London, 223A, 404 (1954).

14. Petch, N.J., "The Cleavage Strength of Polycrystals," The Journal of the Iron and Steel Institute, 174, 25 (1953).

15. Cottrell, A.H., "Theory of Brittle Fracture in Steel and Similar Metals," Transactions, American Institute of Mining, Metallurgical and Petroleum Engineers, 212, 192 (1958).

16. Neuber, H., Kerbspannungslehre (Theory of Notch Stresses), Berlin: Springer-Verlag, AEC TR-4547 (1958).

17. Dieter, G.E., Jr. (3).

18. Tetelman, A.S. and McEvily, A.J., Jr., Fracture of Structural Materials, New York: John Wiley and Sons Incorporated (1967).

19. Beckwith, T.G. and Buck, N.L., Mechanical Measurements, Reading, Mass: Addison-Wesley Publishing Company Incorporated (1961).

20. McGonnagle, W.J., Nondestructive Testing, New York: Gordon and Breach (1961).

21. Durelli, A.J. and Riley, W.F., Introduction to Photomechanics, Englewood Cliffs, N.J.: Prentice Hall Incorporated, 64 (1965).

22. Pook, L.P. and Dixon, J.R., "Analysis of Single-Edge-Notch Tension Speciméns," Fracture Toughness of High Strength Materials: Theory and Practice, The Iron and Steel Institute, Publication Number 120, 45 (1970).

23. Kodak Master Darkroom Dataguide, Kodak Publication Number R-20, Rochester, N.Y.: Eastman Kodak Company (1970).

24. Wilson, E.L., "A Digital Computer Program for the Finite Element Analysis of Axisymmetric Solids With Orthotropic, Non-Linear Material Properties," Unpublished Report, Department of Civil Engineering, University of California, Berkeley (1967).

25. Zienkiewicz, O.C., The Finite Element Method in Structural and Continuum Mechanics, New York: McGraw Hill Publishing Company Limited (1967).

26. Hetenyi, M. (ed.), Handbook of Experimental Stress Analysis, New York: John Wiley and Son Incorporated, 855 (1950).

27. Tetelman, A.S. and McEvily, A.J., Jr. (18,16).

VITA

Glenn M. Kmecz, the son of Andrew Kmecz and Dolores J. Kmecz, was born on January 11, 1947 in St. Louis, Missouri.

He received his primary school education from St. Mary Magdalen Parochial School, and his secondary school education from Bishop DuBourg High School, both in St. Louis, Missouri. He entered the University of Missouri-Rolla in September 1964, and graduated in May 1969 with a Bachelor of Science degree in Mechanical Engineering.

Since September 1969 he has pursued a course of studies toward a Master of Science degree in Engineering Mechanics. While attending graduate school he performed teaching and research duties in the Engineering Mechanics Department in addition to his duties as a Personnel Assistant at the Thomas Jefferson Residence Hall.

He is an associate member of the American Society of Mechanical Engineers, the St. Louis chapter of ASME, an Engineer-in-Training with the Missouri Board for Architects, Professional Engineers and Land Surveyors and is an associate member of the Missouri Society of Professional Engineers.

APPENDICES

APPENDIX A

PSM-1 Calibration and Strength Test

Material - PSM-1

Thickness - 1/4

Scale - 1:1

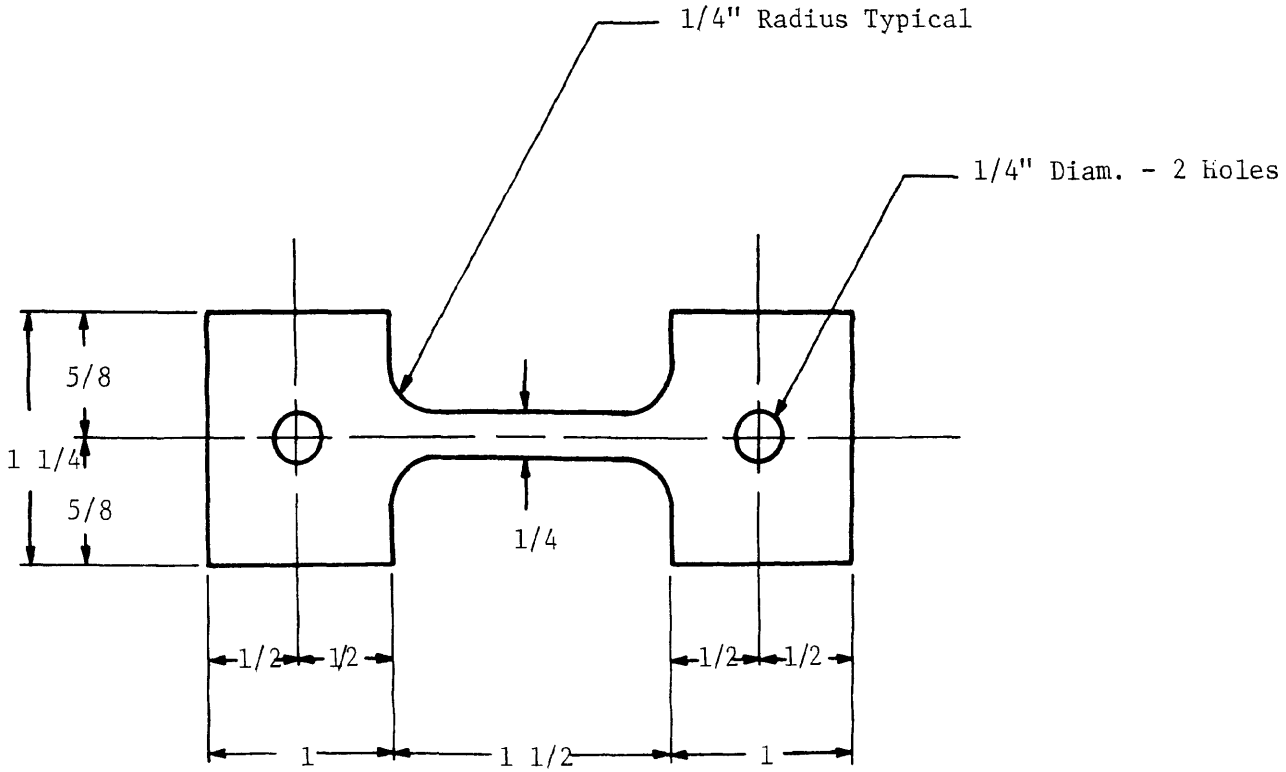

Figure A-1 Tensile Specimen for Strength Test No. 12

TABLE A-I

Strength Test Number 12 Data

Load (lbs.)	Stress (psi)	Strain (μ in/in)
0	0.0	0
20	362.84	1890
40	725.69	3250
60	1088.53	4510
80	1451.38	5620
100	1814.22	6780
120	2177.07	7900
140	2539.91	8910
160	2902.76	10000
180	3265.60	11080
200	3268.45	12170
220	3991.29	13320
240	4354.14	14390
260	4716.98	15610
280	5079.83	16690
300	5442.67	17940
320	5805.52	19140
340	6168.36	20240
360	6531.20	21880
380	6894.05	23200
400	7256.89	24550
420	7619.74	26020
440	7982.58	28160
460	8345.43	29460
480	8708.27	31380
500	9071.12	33700
520	9433.96	36500
540	9796.81	39740
550	9978.23	Gage Failure
578	10486.21	Maximum

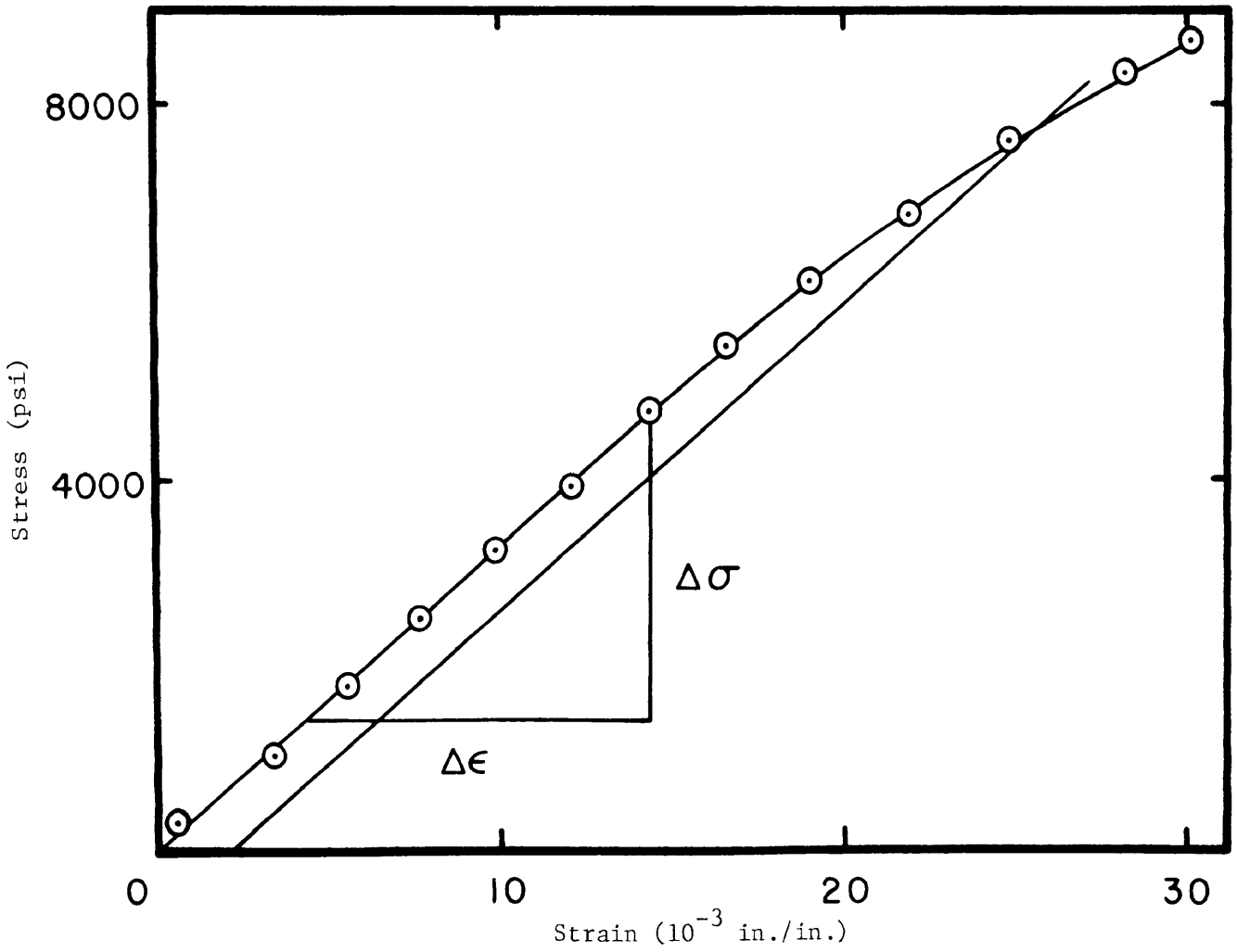

Figure A-2 PSM-1 Strength Test Number 12

Calculations from Strength Test Data

Area for stress calculations

$A = 0.217 \times 0.254 = 0.05512$ square inches

Modulus of elasticity from Figure A-2.

$\Delta\sigma = 4716.98 - 1451.38 = 3265.60$ psi

$\Delta\varepsilon = 15610 - 5620 = 9990$ inches per inch

$E = \Delta\sigma/\Delta\varepsilon = 3265.6/9990 = 326{,}887$ psi

$\sigma_y = 8000$ psi by 0.2% offset method

Material - PSM-1

Thickness - 1/4"

Scale - 1:1

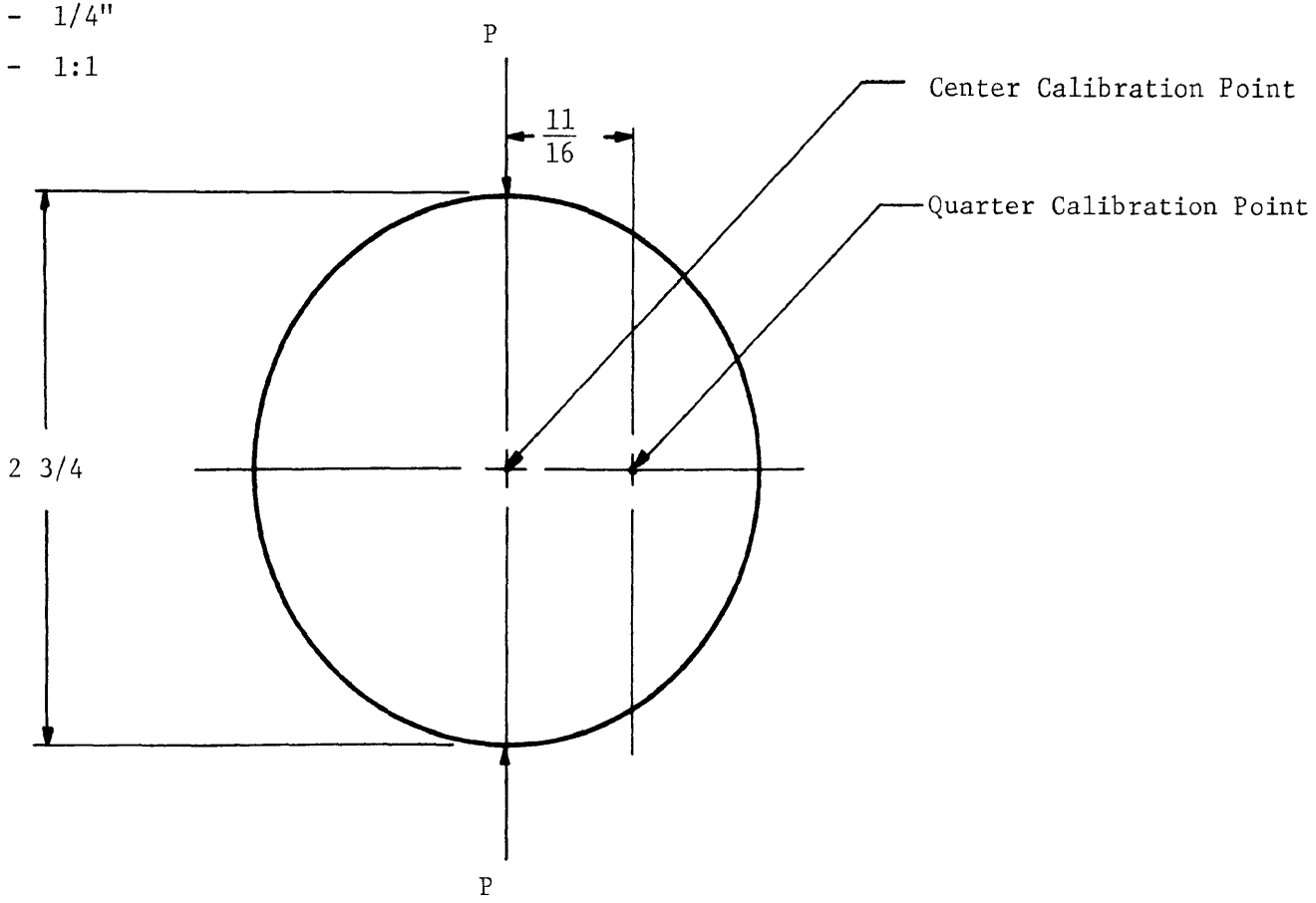

Figure A-3 Calibration Disc

TABLE A-II

PSM-1 Calibration Data

Center Point Data

Fringe Order n	Load P (lbs.)
1/2	20
1	38
1 1/2	58
2	78
2 1/2	97
3	117
3 1/2	134
4	145
4 1/2	148
5	164
5 1/2	197
6	224
6 1/2	240
7	264

Quarter Point Data

Fringe Order n	Load P (lbs.)
1/2	40
1	80
1 1/2	124
2	145
2 1/2	165
3	234
3 1/2	275

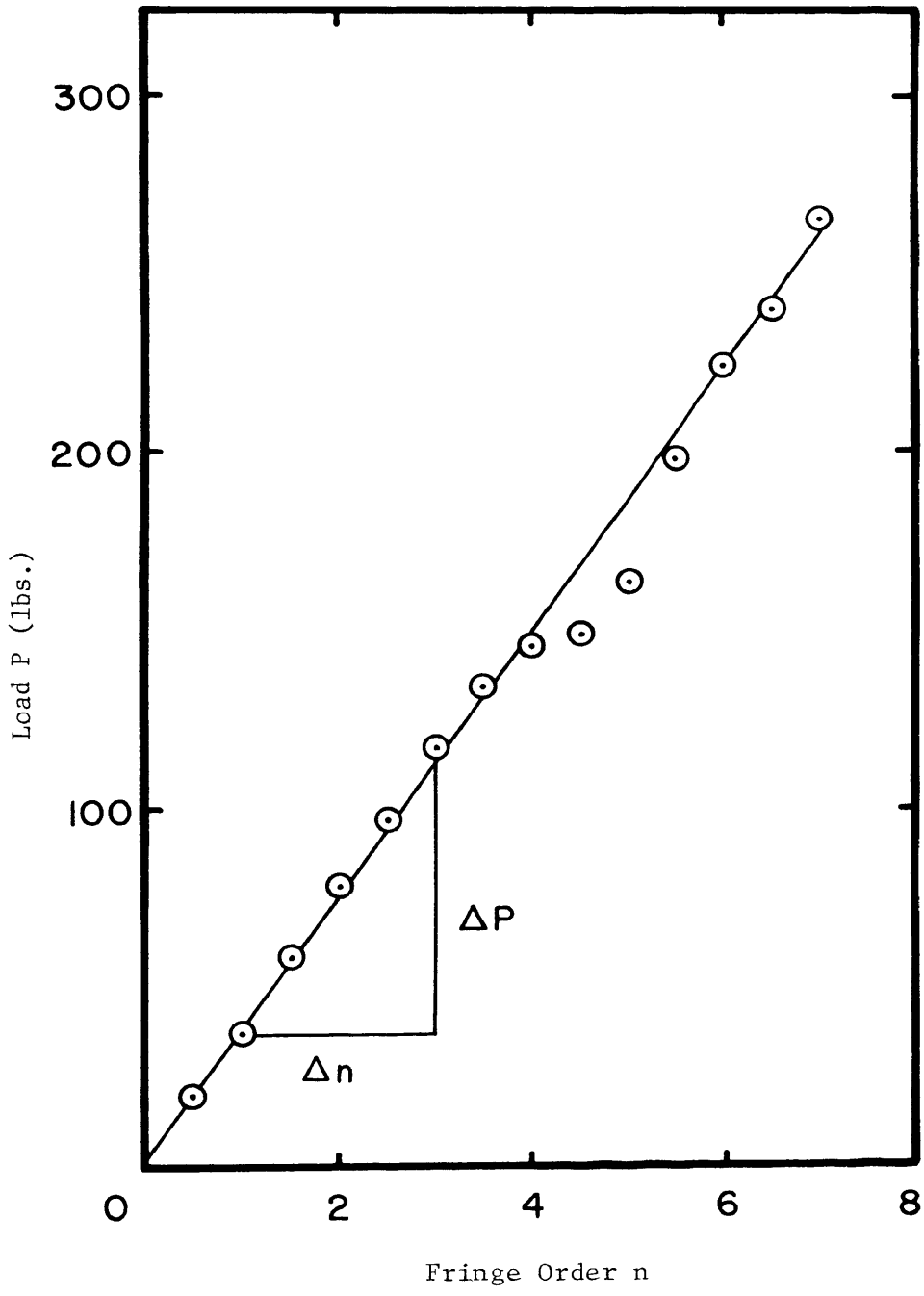

Figure A-4 PSM-1 Center Point Calibration Curve

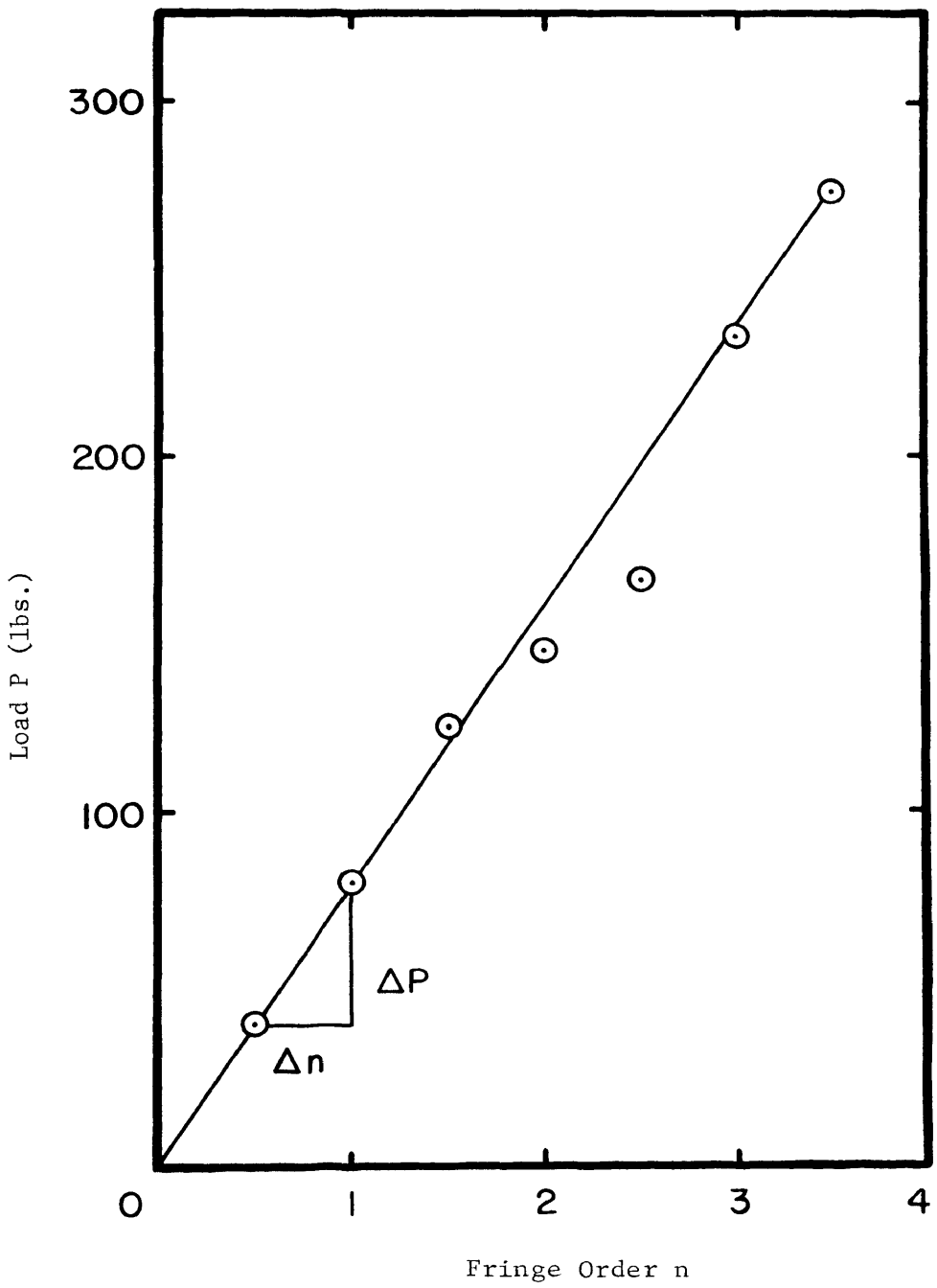

Figure A-5 PSM-1 Quarter Point Calibration Curve

Calibration Calculations

Material Fringe Value from Figure A-4.

$\Delta P = 117 - 38 = 79$ lbs.

$\Delta n = 3 - 1 = 2$

D = Disc Diameter = 2.75 in.

$F = 8/\pi D\ (\Delta P/\Delta n) = (0.926)(79/2)$

$F = 36.577$ psi/fringe/inch

Material Fringe Value from Figure A-5.

$\Delta P = 124 - 80 = 44$ lbs.

$\Delta n = 1.5 - 1 = 0.5$

D = Disc Diameter = 2.75 in.

$F = (0.48)(8/\pi D)(\Delta P/\Delta n) = (0.444)(44/0.5)$

$F = 39.072$ psi/fringe/inch

Average Material Fringe Value

$F_{avg} = (36.577 + 39.072)/2 = 37.824$ psi/fringe/inch

$F_{factory} = 40$ psi/fringe/inch

% deviation = $(40 - 37.8)/40 \times 100 = 5.5\%$

Material fringe value used for photoelastic calculations:

$\underline{F = 37.824 \text{ psi/fringe/inch}}$

APPENDIX B

Finite Element Program Input Structure
(Wilson's Method Modified)

The purpose of this computer program is to determine deformations and stresses within axisymmetric structures of arbitrary shape. The effects of displacement or stress boundary condition, concentrated loads, gravity forces and temperature changes are included. In addition, non-linear material properties are included by a successive approximation technique.

The first step in the structural analysis of an axisymmetric solid is to select a finite element representation of the two-dimension cross-section of the body. Elements and nodal points are then numbered in two numerical sequences each starting with one. The following group of punched cards numerically define the two-dimensional structure to be analyzed.

A. Identification Card - (72H)

Columns 1 to 72 of this card contain information to be printed with results.

B. Control Card - (4I5, 3F10.2, 4I5)

Column	Description	
1-5	Number of nodal points	ex. 233
6-10	Number of elements	ex. 244
11-15	Number of different materials	ex. 1
16-20	Number of boundary pressure cards	ex. 8
21-30	Axial acceleration in Y direction	ex. 0.0
31-40	Angular velocity	ex. 0.0
41-50	Reference temperature	ex. 0.0
51-55	Number of approximations	ex. 1

60 Geometry option 1...Plane

0...Axisymmetric

65 Output interval for plastic analysis

70 Data test option 1...Test data only

2...Run complete program

C. Material property information

The following group of cards must be supplied for each different material:

First card - (2I5, 2F10)

Column	Description	
1-5	Materials identification	ex. 1
6-10	Number of different temperatures	ex. 1
11-20	Mass density of material	ex. 0

Following cards - (8F10.0) One set of cards for each temperature.

First card

Column	Description	
1-10	Temperature	ex. 0
11-20	Modulus of Elasticity-E	ex. 327000
21-30	Poisson's ratio-ν	ex. 0.38
31-40	Thermal expansion coef.-α	ex. 0
41-50	Yield stress-σ_y	ex. 8000

Second card - (See material properties)

Column	Description	
1-10	Stress at point two	ex. 8710
11-20	Stress at point three	ex. 9070
21-30	Stress at point four	ex. 9430
31-40	Stress at point five	ex. 9800

Third card -

Column	Description	
1-10	Strain at point two	ex. 31400
11-20	Strain at point three	ex. 33700
21-30	Strain at point four	ex. 36500
31-40	Strain at point five	ex. 39700

Etc.

D. Nodal Point cards - (2I5, 5F10.0)

One card for each nodal point with the following information

Column	Description	
1-5	Nodal point number	ex. 135
10	Number which indicates if displacements or forces are to be specified	ex. 0
11-20	R - ordinate	ex. 1.150
21-30	Z - ordinate	ex. 0.344
31-40	XR	ex. 0
41-50	XZ	ex. 0
51-60	Temperature	ex. 0

If the number in column 10 is

0 XR is the specified R-load and
XZ is the specified Z-load.

1 XR is the specified R-displacement and
XZ is the specified Z-load

2 XR is the specified R-load and
XZ is the specified Z-displacement

3 XR is the specified R-displacement and

XZ is the specified Z-displacement.

All loads are considered to be total forces acting on a one radian segment. Nodal point cards must be in numerical sequence. If the cards are omitted, the omitted nodal points are generated at equal intervals along a straight line between the defined nodal points. The necessary temperatures are determined by linear interpolation. The boundary code (column 10), XR and XZ are set equal to zero.

E. Element cards - (6I5)

One card for each element

Column	Description	
1-5	Element number	ex. 220
6-10	Nodal point I	ex. 190
11-15	Nodal point J	ex. 189
16-20	Nodal point K	ex. 209
21-25	Nodal point L	ex. 210
26-30	Material identification	ex. 1

Order nodal points counterclockwise around element. Maximum difference between nodal point I.D. must be less than 30. Element cards must be in element number sequence. If element cards are omitted, the program automatically generates the omitted information by incrementing by one the preceding I, J, K, and L. The material identification code for the generated cards is set equal to the value given on the last card. The last element card must always be supplied. Triangular elements are also permissible, and are identified by repeating the last nodal point number

(i.e., I,J,K,L).

F. Pressure cards - (2I5, 1F10.0)

One card for each boundary element which is subjected to a normal pressure (Tensile stresses are negative pressures).

Column	Description	
1-5	Nodal point I	ex. 225
6-10	Nodal point J	ex. 226
11-20	Normal pressure	ex. -53.333

Additional remarks on use of the program:

The previous section contains a schematic description of the program input. The purpose of this section is to explain in greater detail the various portions of the program.

A. Output information

The following information is printed by the program:

1. All input data
2. Nodal point displacements
3. The following stresses and strains are given at the center of each element:
   (a) Effective stress
   (b) Effective strain
   (c) R-stress, Z-stress, θ-stress, RZ-stress
   (d) Maximum and minimum stresses
   (e) Angle locating principal stresses
   (f) Mean stress (pressure)

B. Material properties

Material properties versus temperature are input for each material in tabular form. The properties for each element in the system are then evaluated by interpolation. The mass density of the material is required only if acceleration loads are specified. Listing of the coefficients of thermal expansion are necessary only for thermal stress analysis. The stress-strain curve at each temperature is described by giving the modulus of elasticity, yield strength, and stress-strain coordinates in the plastic region. Linear curves are drawn between each stress-strain point.

C. Skew boundaries

If the number in column 5-10 of the nodal point cards is other than 0, 1, 2, or 3, it is interpreted as the magnitude of an angle in degrees.

APPENDIX C

Photographic Measurements

Procedure for determining actual distances from the photoelastic photographs.

1) Determine to the closest hundredth of an inch the number of grid marks over the image width of the full-view photograph (Figure 14) (i.e. 1.5 inch actual width divided by 16.90 grid marks is 0.0888 inches per grid space).

2) On the close-up photograph (Figure 16) measure the distance between the grid marks shown. The scale factor for the close-up is then:

$$\text{close-up scale factor} = S.F._{cu} = \frac{\text{actual grid distance}}{\text{photo grid distance}}$$

(i.e. 0.0888/2.01 = 0.0442)

Therefore, for any measured close-up distance (d_p) the actual close-up distance (d_a) is:

$$d_a = (S.F._{cu}) \times d_p$$

(i.e. from Table IX for a d_p of 0.130 the d_a is 0.0057)

3) The scale factor for the full-view is found by dividing the actual specimen width (1.5) by the measured width on the full-view photograph.

$$\text{full-view scale factor} = S.F._{fv} = \frac{\text{actual width}}{\text{photo width}}$$

(i.e. 1.5/3.28 = 0.4573)

Therefore, for any measured full-view distance (D_p) the actual full-view distance (D_a) is:

$$D_a = (S.F._{fv}) \times D_p$$

(i.e. from Table IX for a D_p of 0.98 the D_a is 0.4482)